MINISTRY OF EDUCATION AND TRAINING

VIETNAM ACADEMY OF SCIENCE AND TECHNOLOGY

INSTITUTE OF PHYSICS AND ELECTRONICS

PHAM NGOC DIEP

DETECTION AND STUDY OF ULTRA HIGH ENERGY COSMIC RAYS

MASTER THESIS
ATOMIC, NUCLEAR AND PARTICLE PHYSICS
CODE: 60.44.05

SUPERVISOR: PROF. PIERRE DARRIULAT

HANOI - 2006

ACKNOWLEDGEMENTS

First of all, I would like to express my deep gratitude to my supervisor, Prof Pierre Darriulat who has been closely following my work since I joined VATLY in 2003 to do my diploma work. He is also so kind to us not only to take care of our work but also our many living problems. I learn a lot from his lectures, his working style and his experiences that he sometimes kindly tells us about. I take this opportunity to thank him for all that.

I wish to thank my professors from the Institute of Physics and Electronics. During the past two years, I have received from them a lot of knowledge, support and encouragement.

I am grateful to Dr Vo Van Thuan and Dr Dang Quang Thieu who always support us and do their utmost to give us the best condition to learn and do research. I also thank a lot to my colleagues in the group, Thao, Nhung, Dong, with whom I had many useful and helpful discussions. Their kind friendship and their good work are a good motivation for me to do better.

I am deeply indebted to the members of the Pierre Auger Collaboration for their constant interest and support, both material and moral, in the work and progress of our group. In the specific case of the present work, I am particularly grateful to Professors Pierre Billoir, Murat Boratav, Rosanna Cester, Jim Cronin, Antonio Insolia, Giorgio Matthiae, Paul Sommers, Tiina Suomijärvi and Alan Watson for their useful comments. I have personally benefited in this research from support of the Asialink European program and of the University of Catania. The VATLY group in general acknowledges support from the World Laboratory, the French IN2P3-CNRS, the Rencontres du Vietnam, the Odon Vallet fellowships, the Vietnamese Ministry of Science and Technology, the Vietnamese Atomic Energy Commission and the Vietnam Academy of Science and Technology as well as from a few private donators.

Finally, I would like to express my deepest gratitude to my family, my very lovely wife as well as her family, who are always besides me, take care of me, support and encourage me all the time.

Contents

PREAMBLE

Cosmic rays are still today, nearly one century after having been discovered, somewhat of a puzzle. In particular the ultra-high energy (UHE) domain [1], which extends up to some 10^{20} eV, is not really understood: Where are the sources? Which is the acceleration mechanism? Which is the nature of these UHE cosmic rays? Is the region beyond the GZK [2] cut-off (resulting from the opening of the pion photoproduction threshold on the cosmic microwave background photons) populated or not?

The current construction and assembly in the Argentina pampas of a giant cosmic ray detector [3], the Pierre Auger Observatory (PAO), is expected to shed significant new light on these questions. For the first time, a hybrid detector will be in operation on a very large scale, considerably reducing the risk of systematic biases toward high energies. The large collection rate will allow for more than one order of magnitude improvement on the size of the UHE data sample: unless extra-galactic magnetic fields are unexpectedly high, it should be possible to point back to the brightest of the UHE sources.

The aim of the present work is to clarify some aspects of the methods of cosmic ray detection in the UHE range. The PAO, with which we are associated, is used as an illustration. It measures the transverse shower profile using a ground array of water Cherenkov counters (the surface detector array, SD) and the longitudinal shower profile using a set of eyes (the fluorescence detector, FD). Accurate simulations of these detectors are available from the Auger collaboration but they are not what we are after here. Our aim is to get familiar with some important features of both methods of detection with particular emphasis on those that are less obvious.

The thesis is organized in four chapters: the first chapter deals with general features of cosmic rays and some physics of UHE cosmic rays. Since cosmic ray physics is quite new in Vietnam, I would like to describe it in some detail in this part of the thesis. The second chapter describes the two detection methods used in Auger and the experiment itself. The two last chapters are the main part of the thesis. The third chapter deals with event reconstruction using the surface detector and the fourth chapter with event reconstruction using the fluorescence detector which is considered in some depth. This latter study has been submitted to Vietnam Communication in Physics and has been accepted for publication later this year.

Chapter 1

GENERAL INTRODUCTION ON COSMIC RAYS

1.1 A brief history of cosmic ray research

− 1912: On a balloon (Figure 1.1) at an altitude of 5,000 meters, Victor Hess, the founding father of cosmic ray research, discovered "penetrating radiation" coming from space.

− 1932: A debate raged over the nature of cosmic rays. According to a theory of Robert Millikan, they were gamma rays from space hence the name "cosmic rays". But evidence was mounting that cosmic rays were, in fact, mostly energetic charged particles.

Figure 1.1 Victor Hess on his balloon in 1912.

− 1933: While watching tracks of cosmic rays passing through his cloud chamber, Carl Anderson discovered antimatter in the form of the anti-electron, later called the positron.

− 1937: Seth Neddermeyer and Carl Anderson discovered the muon in cosmic rays. The positron and the muon were the first of a series of subatomic particles discovered using cosmic rays – discoveries that gave birth to the science of elementary particle physics. Particle physicists used cosmic rays for their research until the advent of high energy particle accelerators in the 1950's.

− 1938: Pierre Auger, who had installed particle detectors high in the Alps and who was able to use recent development in vacuum tube electronics, noticed that two detectors located many meters apart continued to record coincidences well above the expected random rate. Auger had discovered "extensive air showers (EAS)",

showers of secondary subatomic particles caused by the collision of primary high-energy particles with air molecules. On the basis of his measurements, Auger concluded that he had observed showers with energies of 10^{15} eV – ten million times higher than had been observed before.

− 1949: Enrico Fermi put forth an explanation for the acceleration of cosmic rays. In Fermi's cosmic ray "shock" accelerator, protons speed up by bouncing off moving magnetic clouds in space.

− 1966: In the mid 1960's, Arno Penzias and Robert Wilson discovered that low-energy microwaves permeate the universe. They were immediately identified as the cosmic microwave background (CMB), the remnant radiation from the time when atoms formed, 400,000 yr after the Big Bang. Soon after, Kenneth Greisen, Vadem Kuzmin and Georgi Zatsepin pointed out that high energy cosmic rays would interact with the CMB [2]. The interaction would reduce their energy, so that particles traveling long intergalactic distances could not have energies greater than some 5×10^{19} eV.

− 1991: The Fly's Eye cosmic ray research group in the U.S. observed a cosmic ray event having energy of 3×10^{20} eV. Events with energies in the 10^{20} eV range had been reported during the previous 30 years, but this one was clearly the most energetic.

− 1994: The AGASA group in Japan reported an event with energy of 2×10^{20} eV. The Fly's Eye and AGASA events were higher in energy than any seen before. Where did these two high-energy cosmic rays come from? Neither seemed to point back to an astrophysical object that could produce or accelerate particles of such enormous energies.

− 1995: An international group of researchers begins design studies for a new cosmic ray observatory, the Pierre Auger Observatory (PAO), named in honor of the discoverer of air showers. The new observatory uses a giant array of detectors to detect and measure large numbers of air showers from the very highest energy cosmic rays. Tracing back high energy cosmic rays to their unknown source will advance the understanding of the universe.

1.2 Nature and elemental abundances of cosmic rays

For most of the energy range cosmic rays are known to consist of fully ionized atomic nuclei, mostly protons. For example, the typical composition in the region around 100 GeV (where direct measurements are possible from detectors in space as the high rates allow for the use of detectors of a modest size), 99.8% are charged particles, 0.2% are photons or neutrinos. The charged particle composition is: 98% nuclei, 2% electrons and positrons. The nuclear component is made of: 87% p, 12% α, 0.7% Z=6 to 9, 0.2% Z=10 to 20, 0.1% Z=21 to 30. Cosmic rays' energy density in the universe is of the order of magnitude of the eV/cm^3, similar to those of magnetic fields, of visible light and of CMB photons. However, at variance with those, cosmic rays may carry up to 10^{20}eV per particle, an enormous energy equivalent to that of a tennis ball moving at 100 km/h.

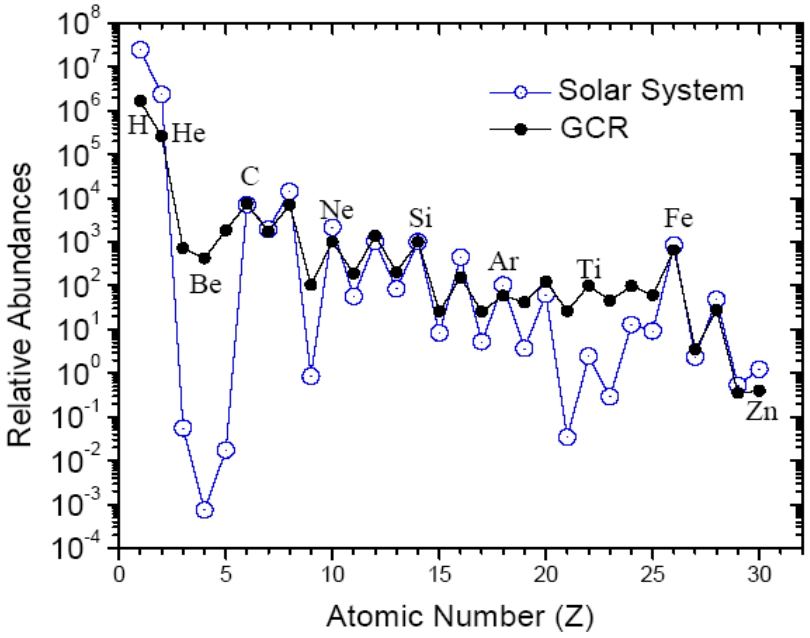

Figure 1.2 Abundance of galactic cosmic rays (full circles). For comparison, the open circles show the abundance of elements in the solar system. The filling of the valleys is understood as being due to spallation reactions.

The galactic cosmic rays (GCR) arriving near the Earth have relative abundances for the more common elements (including C, O, Ne, Mg, Si, Fe, Ni) that are remarkably similar to the relative abundances of these elements in the Solar System (SS). On the other hand, many elements that are rare in the SS (including Li, Be, B, F, Sc, Ti, V) have much higher abundances in the arriving GCR. These

features of the GCR composition, which have been well known for many years, are nicely illustrated[1] in Figure 1.2. The similar abundances of the more common elements is evidence that the composition of the GCR source material, which was accelerated about several 10^6 years ago (the time it takes for a typical cosmic ray to wander around in the Milky Way before reaching the Earth), is very similar to that of the cloud that formed the SS some 5×10^9 years ago. The fact that the GCR abundances fill in the deep valleys in the SS abundances is understood quantitatively as the result of nuclear interactions of cosmic rays with interstellar gas (spallation reactions). For example, interactions of GCR C, N, O result in fragments of lighter elements, ^{3}Li, ^{4}Be, ^{5}B; similarly interactions of Fe produce fragments of ^{21}Sc, ^{22}Ti, ^{23}V.

1.3 Energy dependence of the cosmic ray flux

Cosmic rays have a very broad energy spectrum which extends over 12 decades in energy (from 1 GeV to beyond 10^{11} GeV, hundred million times larger than the highest energy that can be reached with present accelerators) and 32 decades in magnitude of differential fluxes (Figure 1.3).

This spectrum can be well described by a power law: $dN/dE \sim E^{-\gamma}$, where the spectral index γ is equal to 2.7 on average. This law is in fact the convolution of the production at the source with the effect of propagation in the interstellar medium. Taking this into account (and taking a typical 10 My journey for a cosmic ray to reach the Earth from its source) one finds a spectral index between 2 and 2.5 rather than 2.7. In fact small variations are observed: indeed, up to around 10^{15} eV the spectrum can be described by a γ of 2.7; by a γ of 3.0 up to around 10^{18} eV; then again by a γ of 2.7 higher up. These two breaks are usually referred to as the "knee" and the "ankle" respectively. Cosmic rays having energy above the ankle region are called ultra-high energy cosmic rays (UHECR). The rate of cosmic rays above this region is extremely small, about 1 *particle/ km^2/ year* at the ankle.

[1] Both GCR and SS abundances are normalized, by convention, to Si = 10^3. GCR abundances for elements ^{3}Li - ^{28}Ni are CRIS (Cosmic Ray Isotope Spectrometer launched aboard NASA's Advanced Composition Explorer in 1997) measurements during solar minimum, August 1997 through April 1998, showing relative fluxes at 170 MeV/nucleon. The GCR abundances for the relatively rare elements ^{29}Cu and ^{30}Zn are also from CRIS during solar minimum, but include the full CRIS energy range for these elements, 150 - 550 MeV/nucleon. The GCR abundances for H and He are for solar minimum at 170 MeV/nucleon, derived from measurements by the balloon-borne instrument BESS (Balloon-borne Experiment with a Super-solenoidal Spectrometer) and the GSFC (Goddard Space Fly Center) instrument on the IMP-8 spacecraft.

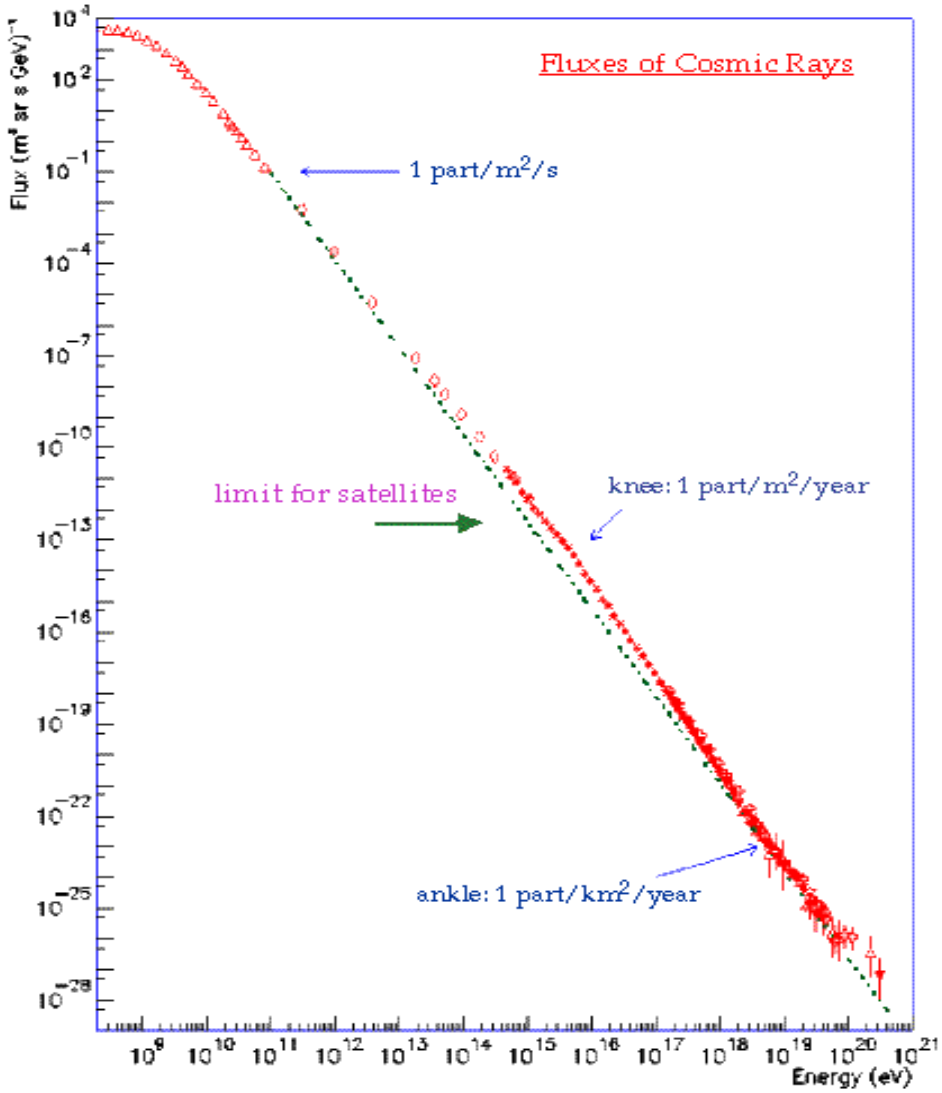

Figure 1.3 All-particle energy spectrum from a compilation of measurements of the differential energy spectrum of CR. The dotted line shows an E^{-3} power-law distribution for comparison. Approximate integral fluxes are also shown.

Cosmic rays with energy up to the knee (around 10^{15} eV) are believed to be accelerated in the Milky Way by diffusive shock acceleration in supernova remnants (SNR). We still need more data to understand the changes of slope in the spectrum. At the ankle, the cosmic rays' energy spectrum starts receiving contributions (soon dominant) from extra-galactic cosmic rays which have energies high enough to escape from the confinement of the galactic magnetic field. In Figure 1.4 (where the spectrum is multiplied by E^3 for convenience), the breaks at the knee and ankle are clearly visible.

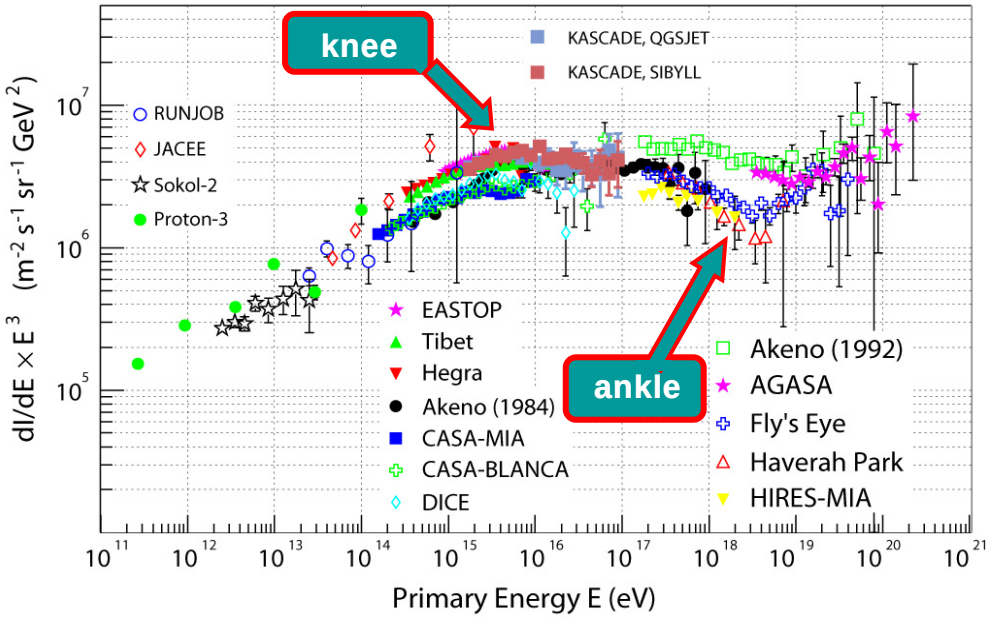

Figure 1.4 A compilation (from data and simulation) of cosmic ray spectrum multiplied by E^3, showing the knee and ankle.

1.4 The GZK effect

The main physics goal of the PAO is a study of the upper end of the energy spectrum. It will provide an accurate measurement of the flux that will settle the GZK question, will hopefully identify the brightest sources and clarify the nature − protons, nuclei, or else − of the UHECRs.

Above 10^{20}eV or so one expects the spectrum to be cut off (this is known as the Greisen-Zatsepin-Kuzmin or GZK cutoff) because of the interactions between the cosmic ray particles with the 2.7K Cosmic Microwave Background (CMB) photons [2]. In the case of incident protons, the resulting distortion of the primary spectrum depends on several parameters: the reaction considered, essentially $p\gamma \rightarrow \pi^0 p$ or $\pi^+ n$ either directly or via Δ^+ production; the distribution of the CMB photons in energy ε (Planck spectrum) and angle (isotropic); the cross-section of the reactions being considered; the primary proton spectrum. For a given initial state, defined by the energy E of the primary proton and the angle θ between its momentum and that of the CMB photon, the kinematics of the reaction gives $M_p \Delta m \cong E\varepsilon(1-\cos\theta)$ where Δm is the difference between the mass of the final state and the proton mass, namely either the pion mass (140 MeV) or the difference between the

mass of the Δ resonance and the proton mass (290 MeV). For a given Δm, the distribution in incident energy of the interacting protons is obtained by integration over ε and θ with weights accounting for the CMB distributions and for the value of the cross-section. Moreover, the final distortion implies another convolution of the proton energy loss over the initial proton spectrum. To get a crude order of magnitude estimate of the effect, we may replace the Planck spectrum by a δ-function at 10^{-3} eV, take $cos\theta$=0 on average, and assume that any interacting proton is essentially lost (namely that its energy is shifted to a much lower range where its contribution to the spectrum is negligible). This results in an abrupt threshold at $M_p\Delta m/\varepsilon = 3\times10^{20}$ eV and 1.5×10^{20} eV for Δ and π production respectively above which all protons that have interacted are suppressed. The fraction of such protons depends upon the reaction cross-section and the distance of the source to which the target thickness, and therefore the interaction rate, is directly proportional. The exact calculation [4], taking all above factors into account, gives instead distortions illustrated in Figure 1.5. An essential result is that for source distances in excess of 50 Mpc the spectrum is effectively cut-off.

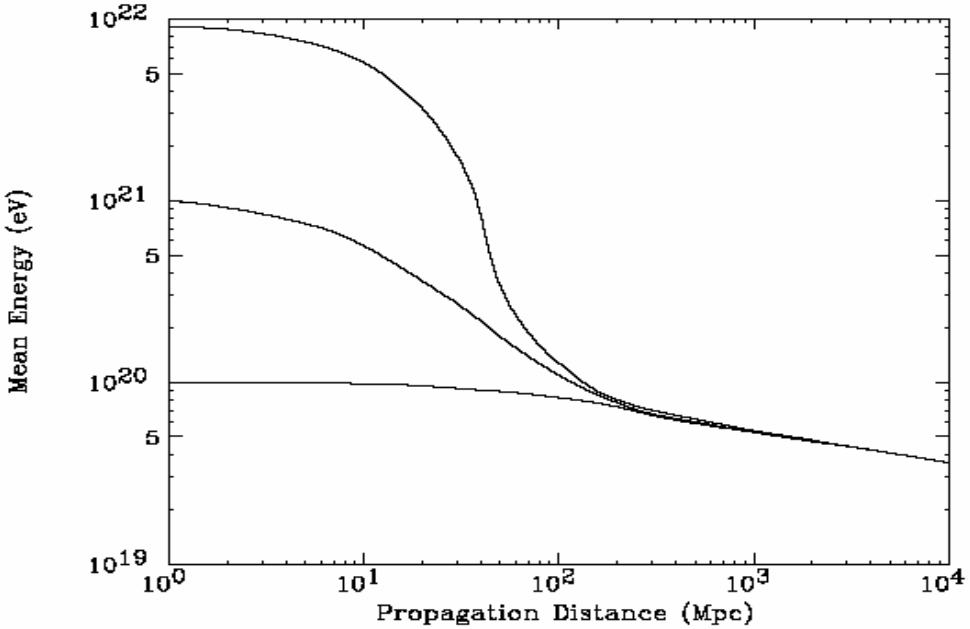

Figure 1.5 Mean energy of protons as a function of propagation distance through the CMB. Curves are for energy at the source of 10^{22} eV, 10^{21} eV, 10^{20} eV respectively.

It is only for sources distant by less than 30 Mpc or so, that the effect of the cut-off is small. The observation of UHE protons above 10^{20}eV or so would

therefore imply that they originate from sources located in the Milky Way or other nearby galaxies in the local cluster, restricting severely the possible acceleration mechanisms.

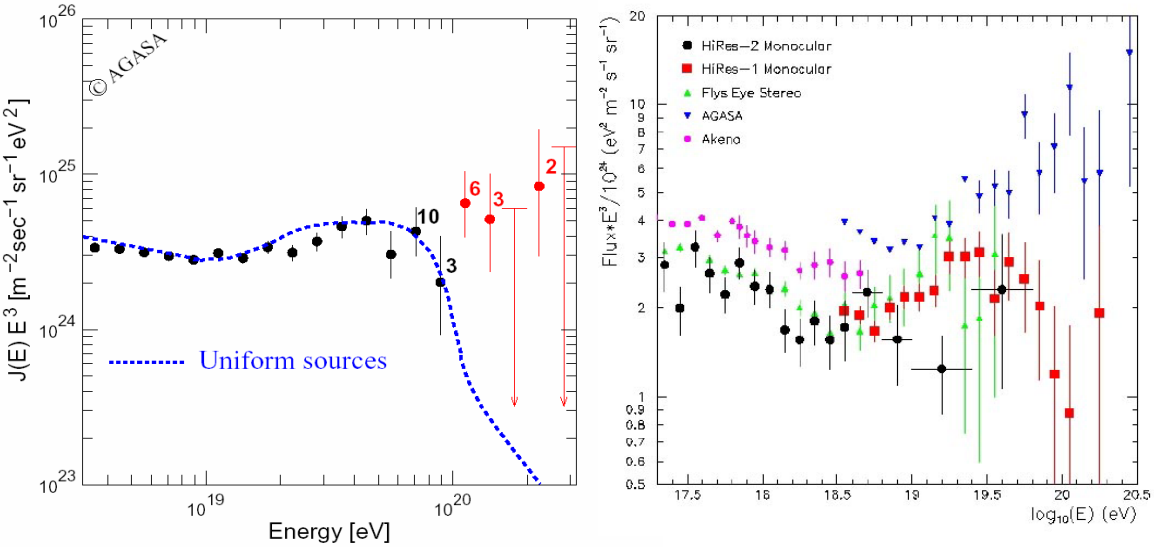

Figure 1.6 Data measured in the region of GZK.

Figures 1.6 and 1.7 show the data observed in the GZK region from different experiments. While the data from HiRes (the full squares in Figure 1.6 on the right) seem to support the GZK prediction, those from AGASA do not. This issue is currently controversial. Recent data from Auger [13] are shown in Figure 1.7 and show that this experiment will soon settle the issue.

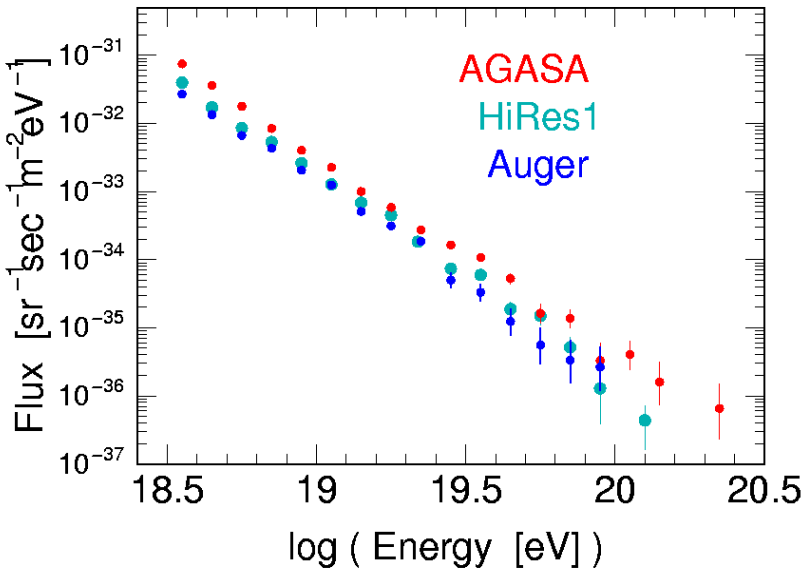

Figure 1.7 Auger data vs Hires1 and AGASA.

1.5 Diffusive shock acceleration: an elementary description

Consider a cloud, say a SNR, expanding and moving (at relativistic velocities) into the surrounding inter stellar medium (ISM) (see Figure 1.8). The density of the cloud is supposed to have become so low that the particle mean free paths are large enough for collisions to be always safely ignored. Moreover we assume that both the cloud and the surrounding ISM are fully ionized, say H_{II} to make it simple, namely electrons and protons. The only relevant interaction between the particles is via magnetic fields. Both the ISM and the cloud have a history from which they have probably inherited some local collective motions sufficient for having trapped some fields. While expanding, the fields have decreased in amplitude to a microgauss scale or so. Original hydrodynamical turbulences have left their imprint in the form of field inhomogeneities. In the process of dilution some field line reconnection has taken place. We may therefore expect a very complex and erratic magnetic field structure in both the cloud and the ISM but we do not really understand how to describe it. We next assume that nearly

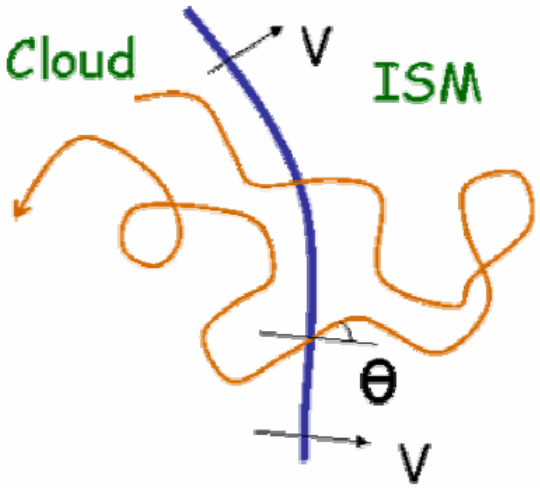

Figure 1.8 Diffusive shock acceleration. The random walk of the accelerated cosmic particle is the result of magnetic fields, not of collisions on ISM particles.

relativistic particles, say protons, having energies very much higher than the respective energies of the thermal protons of the ISM and cloud (otherwise how could we tell them apart?), are present in the region. We call them "cosmic particles" to distinguish them from the thermal particles. They are the particles that will be accelerated further in the process. We assume that the interface between the cloud and the quiet ISM, called the "shock", is sufficiently thin to guarantee that cosmic protons entering it at not too large an angle of incidence will traverse it. We

also assume that the magnetic field structures in the ISM and in the cloud are such that a cosmic proton coming from the shock will interact in a random walk with the magnetic field inhomogeneities and have a fair chance to return to the shock and traverse it once more. Two points are essential here. First, in its "interactions" with the magnetic fields, which are nothing more than magnetic bends, the cosmic particle changes momentum but it retains its energy. Second, we can talk of a "cloud rest frame" and of an "ISM rest frame" moving toward each other at velocity V. A cosmic particle, having energy E and momentum p in the rest frame of the medium in which it is, reenters the shock at an incidence θ_{inc}. It comes out in the other medium with energy $E'=\gamma\beta\ p\ cos\theta_{inc} + \gamma E$ with $\beta = V/c$ and $\gamma^2=1/(1-\beta^2)$. To first order in V/c, $E'= E+\beta\ p\ cos\theta_{inc}$, and, as the cosmic particle is relativistic, $E \sim p$, hence an energy gain (it is always a gain, never a loss, whatever the direction of the shock traversal) $\Delta E/E= \beta\ cos\theta_{inc}$. Depending on assumptions $< cos\theta_{inc} >$ may take different values; a reasonable model gives 2/3. Then, after n pairs of traversals, the energy has increased to $E_n=E_0(1+4\beta/3)^n$. However, at some stage, the cosmic particle may ultimately escape the system and acceleration will then stop. Writing P_{esc} the escape probability (assumed to be E-independent) the fraction of remaining cosmic protons after n cycles is simply $(1-P_{esc})^n$.

Hence $dN/dE=-NP_{esc}/(4E\beta/3)$, namely $N=N_0\ (E/E_0)^{(-Pesc/(4\beta/3))}$. This is a power spectrum having an index $\nu= P_{esc}/(4\beta/3)$. As P_{esc} is more or less proportional to β, the spectral index may be expected to take similar values in different configurations. Putting numbers in for the size and age of the SNR one finds that this mechanism is in principle able to accelerate particles up to 100 TeV or so [5]. Its extension to shocks occurring in AGN's might then be able to explain the highest cosmic ray energies, around 10^{20}eV. Multitraversals are essential for the mechanism to work. As they are due to stochastic scattering on field inhomogeneities, it implies that the Larmor radius of the cosmic particles (that of course keeps increasing during the acceleration phase) be large with respect to the shock thickness and at least of the same order of magnitude as the characteristic scale of the magnetic field inhomogeneities (this is necessary for making it meaningful to describe the Brownian motion as occurring in the rest frame of the medium concerned). Note that the ISM and SNR plasmas in which the cosmic particles are moving are themselves subject to proper oscillation modes that may be resonantly excited in particular conditions. Finally one should mention that, like

most other mechanisms that have been studied, diffusive shock acceleration requires that the accelerating site has a large size and is the seat of a large magnetic field. Quantitatively it is the product of these two quantities that defines the maximal attainable energy. This is illustrated in Figure 1.9, usually referred to as the "Hillas plot".

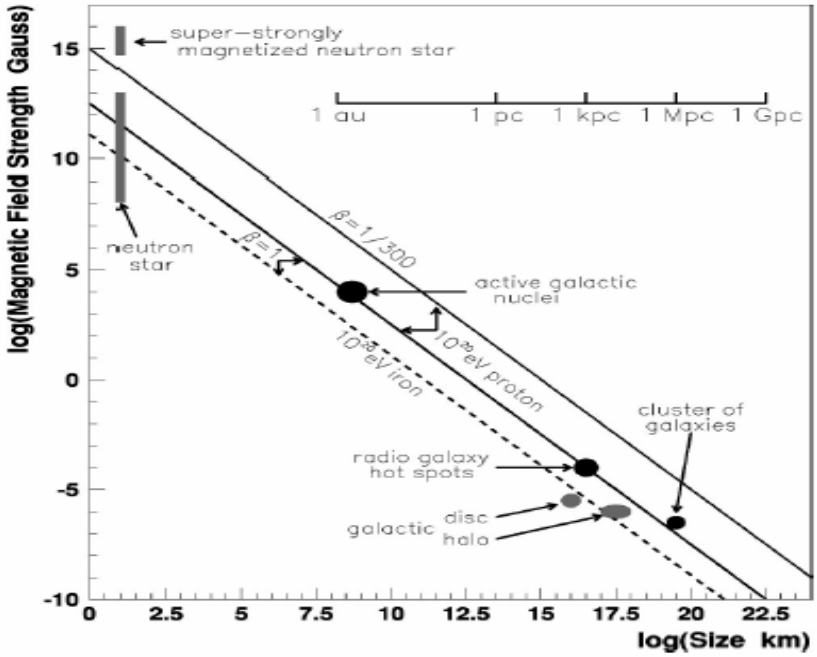

Figure 1.9 Hillas plot showing the minimal value of the product BL (magnetic field × size) for accelerating a proton to 10^{20} eV. The limit is shown as a line in the log-log plot. A few candidate sites are indicated.

Chapter 2

DETECTION OF UHECR, THE PIERRE AUGER OBSERVATORY

2.1 Extensive air showers

When a high energy cosmic ray enters the Earth atmosphere it interacts with molecules in the atmosphere and looses energy. The secondary particles produced in the interaction continue to interact with molecules in the atmosphere and create new generations of particles. All the charged particles produced loose energy by ionization (or to a much lesser extent excitation) of the atmospheric molecules. This process repeats until the average energy of secondary particles equals that required to create new particles. At this stage the total number of shower particles reaches its maximum and starts decreasing down to zero. The set of particles produced is called a shower. Such a shower contains three components:

− *Hadronic component*: Each of the interactions of hadronic secondaries (mostly pions and kaons) produces a new generation of high energy hadrons which in turn interact or decay.

− *Electromagnetic component*: At each interaction, 1/3 of the incident particle energy goes into neutral *pions*. After a very short time, these *pions* decay into photons that initiate an electromagnetic cascade via pair creation and bremsstrahlung. Note that a very high energy shower, implying a very large number of generations, spends nearly all its energy in the electromagnetic component as $1/3+(1/3)(2/3)+(1/3)(2/3)^2+...=1$. This however ignores the energy taken away by the third component.

− *Muon and neutrino component*: charged *pions* and *kaons* may decay into *muons* and *neutrinos* if their decay length is short enough in comparison with the interaction length. Muons radiate little energy and have a long lifetime: they often will reach ground. Neutrinos simply escape, undetected.

The shower develops along the trajectory of the primary particle longitudinally and transversally. The shower front is nearly planar, with a small curvature, and moves at the speed of light.

2.2 The Pierre Auger Observatory

The Pierre Auger Observatory has been conceived to measure the flux, arrival direction distribution and mass composition of cosmic rays from 10^{18}eV to the very highest energies with high statistics over the whole sky. To do that, the Observatory will have detectors located at two sites, one in each of the Northern and Southern Hemispheres.

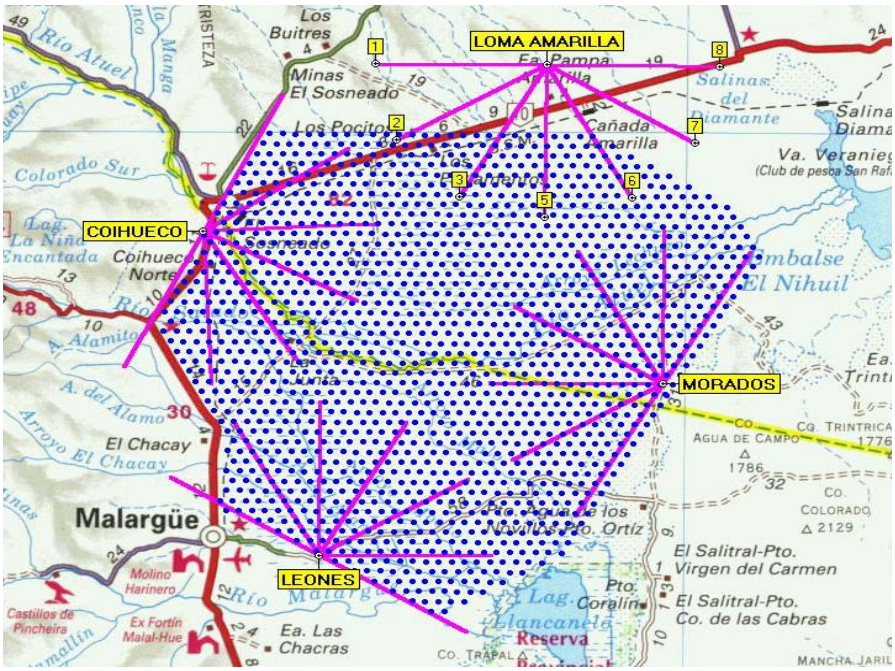

Figure 2.1. Pierre Auger Observatory's outline.

The Southern site started being constructed in 1999 in Malargue pampa, Argentina and should be completed in 2007. The PAO is the first and largest hybrid detector ever built to study cosmic rays. It covers an area of 3000 km^2. It consists of two kinds of detectors, each using a different technique, namely surface detectors and fluorescence detectors. The arrangement of detectors in the PAO is shown in Figure 2.1 above. There are 1600 water Cherenkov counters located at the vertices of a triangular array of 1.5 km mesh size. There are four stations of six fluorescence detectors each (eyes). Each station looks at the center of the surface array and covers a field of view of 180^0 in azimuth and about 28^0 in zenith angle.

2.3 The surface detector

A schematic picture of a surface detector unit is shown in Figure 2.2. It is a Cherenkov counter consisting of a cylindrical molded polyethylene tank, 3.6 m in diameter and 1.55 m high, enclosing a liner filled with 12000 liters of high purity water (1.20 m in height). Contrary to scintillator plates used in other arrays (such as AGASA) these counters offer a cross section to the incident shower particles that has little dependence on the incidence angle.

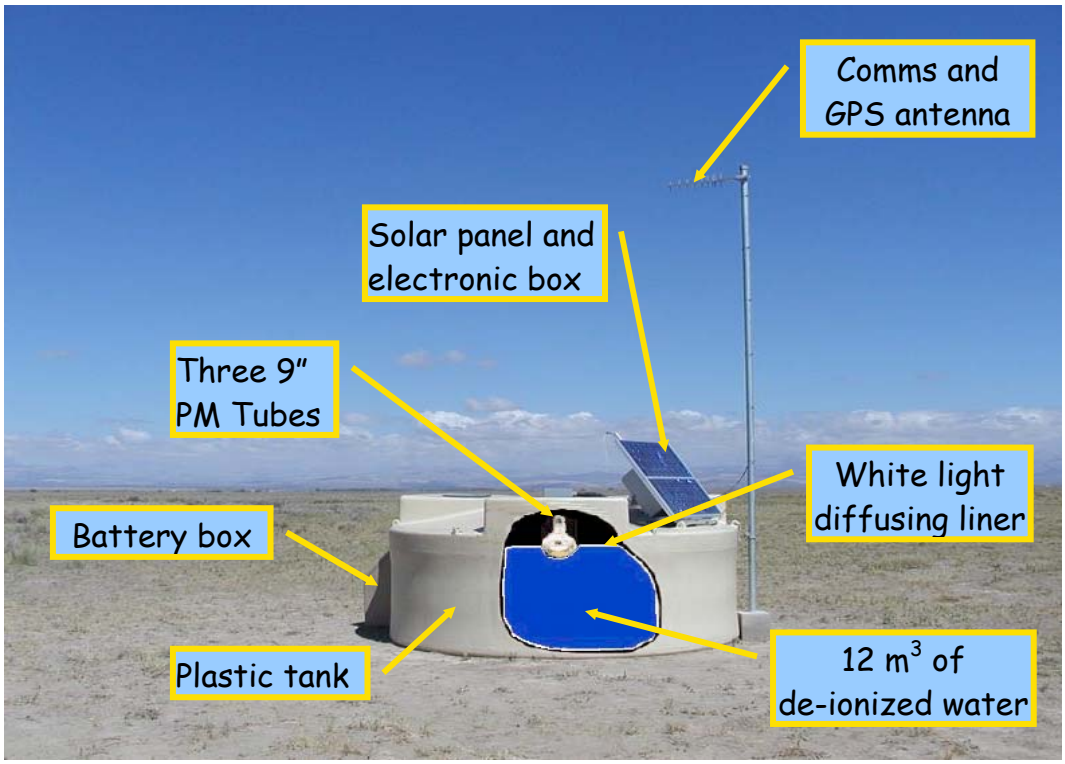

Figure 2.2 Structure of a water Cherenkov counter.

The Cherenkov light is observed through three transparent plastic windows set into the top surface of the liner. Signals from PMTs glued onto the windows are read by local electronics modules. Power is provided by batteries connected to two solar panels, and time synchronization relies on a commercial GPS receiver. A specially designed radio system is used to provide communication between the surface detectors and the central computers of the Observatory. Each tank forms an autonomous unit, recording signals from the ambient cosmic ray flux, independent of the signals registered by any other tank in the surface detector array. A combination of signals clustered in space and time is used to identify a shower. The

SD array has a 100% duty cycle and a well-defined aperture that is independent of energy above 10^{19} eV. Its response is largely independent of weather conditions.

Surface array detectors have been often used to detect cosmic ray showers because of a large number of advantages, including their stability, large detection areas and duty cycle. The arrival time of the particles in the shower can be measured with a good resolution leading to an excellent reconstruction of the primary particle direction ($\pm 1.5^{o}$). Besides, ground array detectors have a well defined aperture resulting in a straight forward determination of their acceptance and of the cosmic ray spectrum.

However, since ground array experiments detect a sample of the shower development at a single depth, the energy reconstruction can not be derived in a direct or calorimetric way. In fact, the energy of the primary particle must be reconstructed from the lateral distribution of particles in the shower. In 1969, Hillas et al. [6] showed that at a given distance of the shower axis, the fluctuations of the lateral distribution function (LDF) due to intrinsic shower fluctuations are minimized. In subsequent works [7], it was also shown that the measured signal fluctuation is very small at a certain distance in spite of the different types of primary particles and of models used to define the LDF.

The distance at which the fluctuations reach their minimum is a convolution of the intrinsic shower-to-shower fluctuation, the experimental uncertainties and the reconstruction procedures. One very important experimental input is the array spacing which mathematically determines the properties of the LDF fit [8]. The Haverah Park experiment [9] used water Cerenkov tanks and determined the distance of least fluctuation to be 600 meters. Operating with the same ground array technique, the Pierre Auger Observatory [3] has determined the distance of least fluctuation to be 1000 meters. Therefore, the LDF in Auger has the form [3]:

$S(r(km)) = S(1000)r^{-\upsilon}$, for zenith angle < 60^{o}, where $\upsilon = 4.08 - 1.26 \sec\theta$.

S(1000), the signal at 1000 m from the shower axis, is used to estimate the primary energy. The relationship between the energy in EeV (1 EeV ≡ 10^{18} eV) and S(1000) currently adopted in Auger is

$$E(EeV) = 0.12(\sqrt{1 + 11.8(\sec\theta - 1)^2}\, S(1000))^{1.05}.$$

2.4 The fluorescence detector

2.4.1 The PAO eyes

The first fluorescence detectors were two fly's eyes [10] that were operated in Utah between 1981 and 1992. Together, they consisted of some hundred mirrors looking at the whole sky and focusing light on arrays of photomultiplier tubes, over a thousand in total.

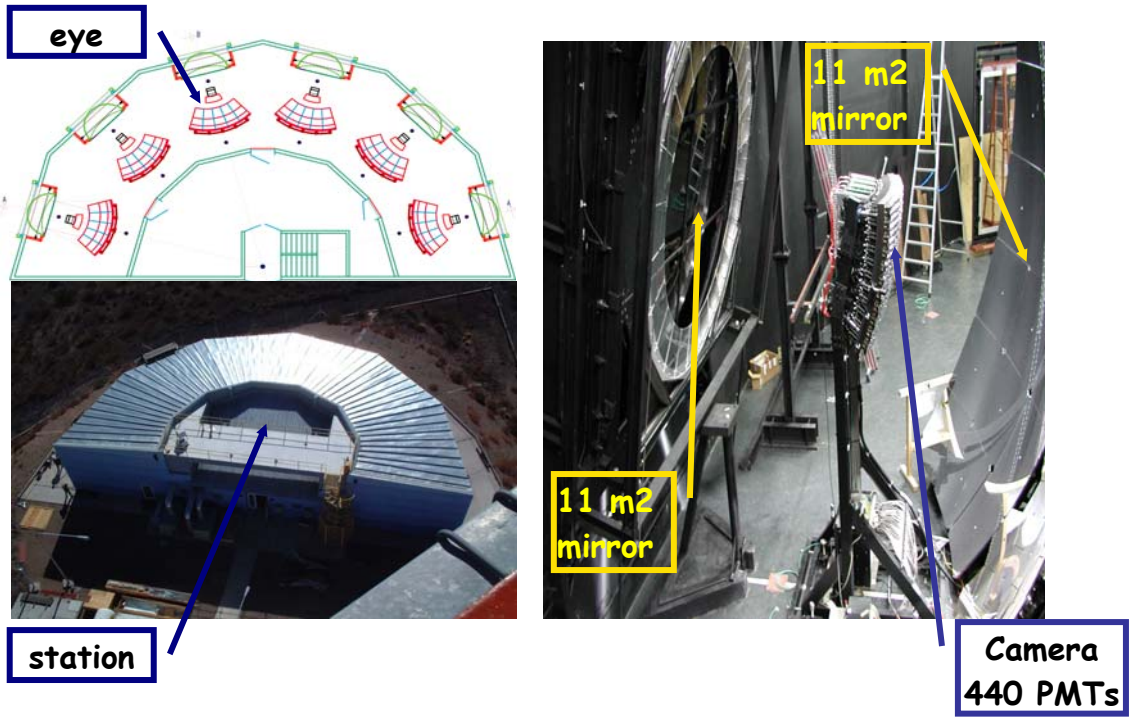

Figure 2.3 Auger Fluorescence Detector

The experience gained in this pioneering work made it possible to design optimally its successors: HiRes [11] and the PAO [3]. While HiRes consists again of two fly's eyes, separated by a distance of 12.5 km, the Auger eyes (shown in Figure 2.3) match the configuration of the surface detector array in order to optimize the efficiency of hybrid detection: four stations of six eyes each are located on the periphery of the array. Each eye covers a field of view of approximately $28^{o}\times30^{o}$, from 62^{o} to 90^{o} in zenith angle and 180^{o} in azimuth for each station. An eye includes a UV filter and shutter to protect the detector, a 3.5×3.5 m^2 spherical mirror and an array of 440 photomultiplier tubes at its focus. The phototubes have hexagonal photocathodes closely packed together and special light guides allowing

for negligible light loss at their junctions. Each phototube (pixel) has a field of view of approximately $1.4^{o}\times1.4^{o}$ and its signal is recorded in a fast analogue to digital converter in 100 ns slices. This latter feature is essential in achieving a high accuracy. Additional equipment is used to measure and monitor the light attenuation in the atmosphere (the attenuation length is of the order of 15 km) and to calibrate and monitor the light collection efficiency of the detector. Figure 2.4 shows the pixel patterns observed by two successive eyes as well as the shower geometry.

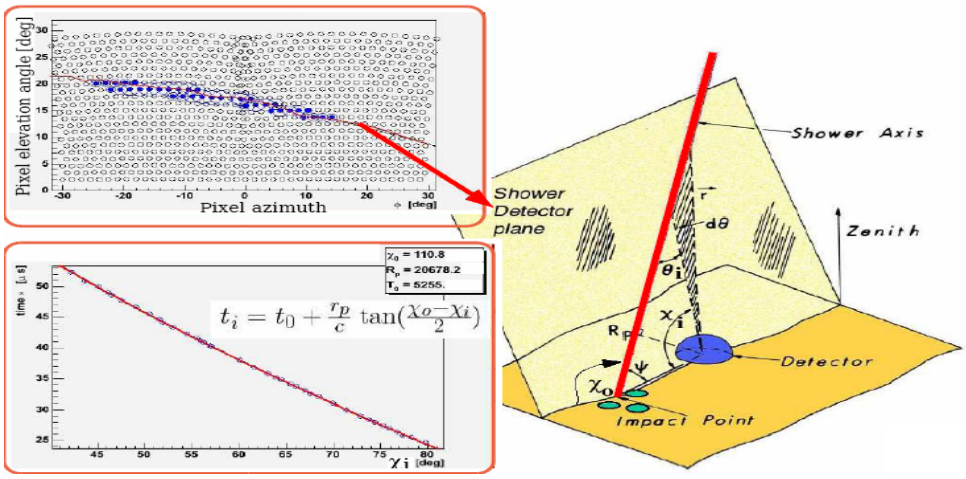

Figure 2.4: On the left, the upper panel shows an example of pixel patterns observed in two successive eyes. In the lower panel, the measured pixel time is plotted as a function of observed angles. On the right, the picture shows the shower geometry.

2.4.2 Longitudinal development of an air shower

The longitudinal development of an air shower is described by its profile. On average, the longitudinal profile of a shower induced by a given primary cosmic ray is a universal function of the depth of atmosphere traversed. It is well described by a Gaisser Hillas function [11].

$$S(X) = S_{\max}\left(\frac{X - X_1}{X_{\max} - X_1}\right)^{(X_{\max}-X_1)/w} e^{(X_{\max}-X)/w} \qquad (1.1)$$

where $S(X)$, X_1, S_{max}, X_{max} and w are the shower size at depth X, the depth of the first interaction, the maximum value of the shower longitudinal profile, the depth at which this maximum is reached and a quantity close to the interaction length for the

primary particle, usually taken equal to 70 g/cm^2, respectively. On average, the difference $X_{max}-X_1$ depends on the energy and on the nature of the primary, X_1 depends only on the nature of the primary. X_{max} increases logarithmically with energy in GeV [12]:

$$X_{max}= 107\ [g/cm^2] + 67[\ g/cm^2] \times log_{10}E \qquad (1.2)$$

This correlation is illustrated in Figure 2.5 obtained from experiments and simulations. For the development of showers initiated by a nucleus of energy E and mass A, it is found that X_{max} is approximately expressed [14] as $X_{max}=(1-B)X_0(\ln E/\varepsilon - \langle lnA\rangle)$, where X_0 is the radiation length in air (37.1 g/cm^2), ε is the critical energy in air (81 MeV), B is 0 for a pure electromagnetic cascade and less than 1.0 by an amount that depends on the hadronic interaction model for a hadronic cascade; in practice, at a given energy, $X_{max}(p) - X_{max}(Fe)$ ~100g/cm^2 (as shown in Figure 2.6).

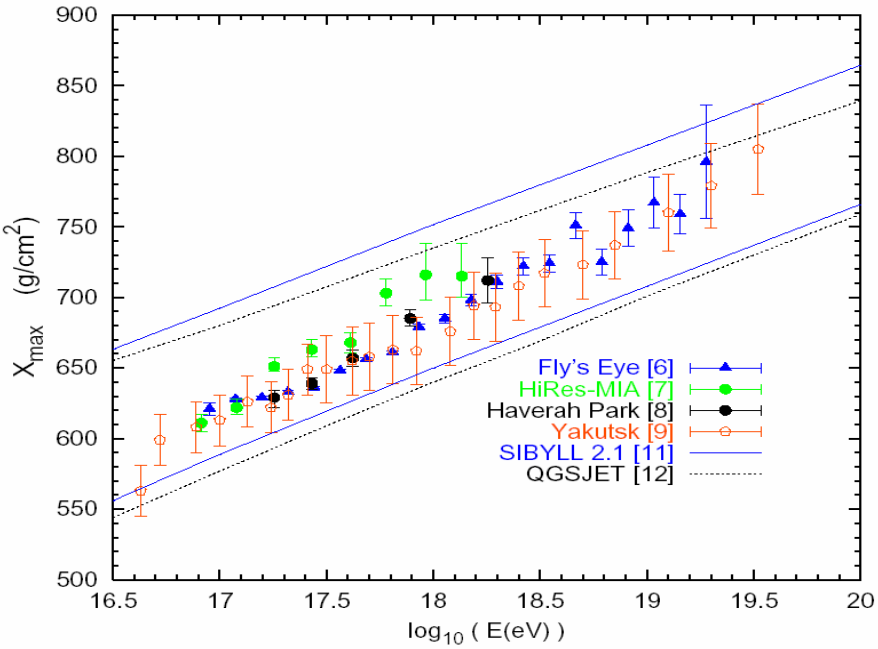

Figure 2.5 The correlation between X_{max} and $log_{10}E$, E being the energy of the primary cosmic ray, as obtained from various experiments and simulations.

The longitudinal profiles of proton-showers (red) and iron-showers (blue) obtained from a sample of simulated events at 10^{19} eV are shown in Figure 2.6. Larger fluctuations are obtained with primary protons and a shift in X_{max} of about 100 g/cm^2 is clearly visible.

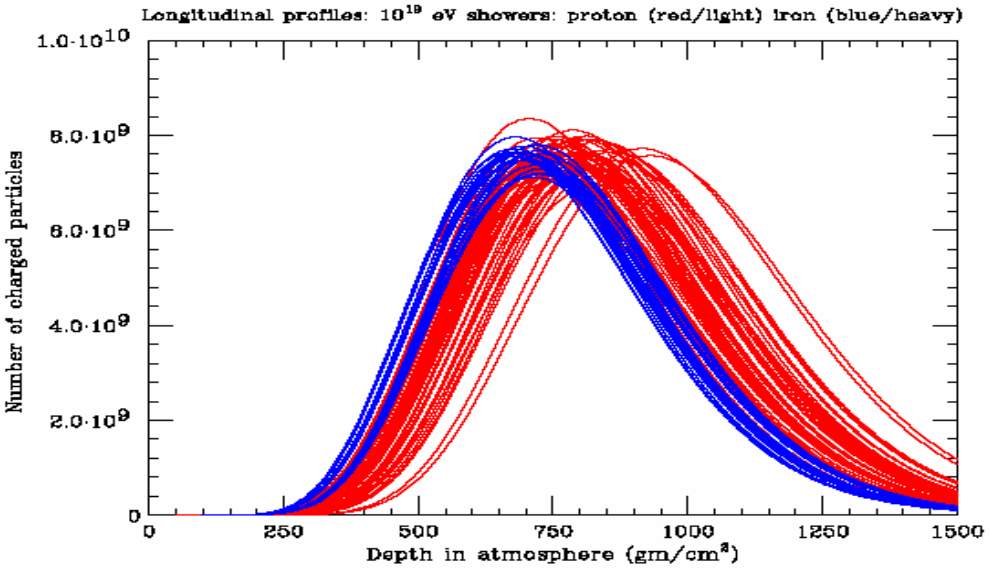

Figure 2.6: Longitudinal profiles of simulated proton (red) and iron (blue) showers with a primary energy of 10^{19} eV.

The energy carried by the electromagnetic component (E_{em}) is evaluated by the track length integral as

$$E_{em} = \frac{(critical\ energy\ of\ electron\ in\ air)}{(radiation\ length\ of\ electron\ in\ air)} \times (total\ track\ length\ in\ g/cm^2)$$

$$= (2.18\ MeV) \times (total\ track\ length\ in\ g/cm^2)$$

The fraction of energy passed to the electromagnetic component for hadronic showers varies with primary energy and mass and is about 80–90% of the total energy for 10^{19} eV. In the case of proton primaries, the number of electrons at maximum shower development fluctuates by about 10% from shower to shower. The total track length is determined by the integral $\int N_e(x)dx$, making an assumption about the shape of the cascade curve after the observation level. Allowing for lost energy (e.g. neutrinos) and particles traveling not quite parallel to the shower axis, the primary energy has been estimated [1] as

$$E=(2.65MeV) \times \int N_e(x)dx.$$

To estimate the energy resolution of the shower as measured by the fluorescence method, the following factors must be taken into account [10]: the air fluorescence efficiency, the subtraction of direct and scattered Cherenkov light, the attenuation and scattering of photons, and uncertainties in the geometrical reconstruction.

Chapter 3

EVENT RECONSTRUCTION USING THE SURFACE DETECTOR

We have written a program to reconstruct the direction and the front curvature of Auger showers. To test this reconstruction program, a Monte Carlo has been written that: generates showers and calculates the response of the Auger array. By this way, the reconstructed shower parameters and the generated shower parameters can be compared and the quality of the reconstruction program can be evaluated.

3.1 Geometric reconstruction

The shower geometry is described in simple terms by seven parameters: the space-time coordinates of the impact on ground of the shower front on the shower axis (x_0 , y_0 , z_0 , t_0), the zenith angle θ and azimuth φ of the unit vector $\vec{u}$ directed along its axis, and the curvature C of the shower front assumed to be spherical and infinitely thin.

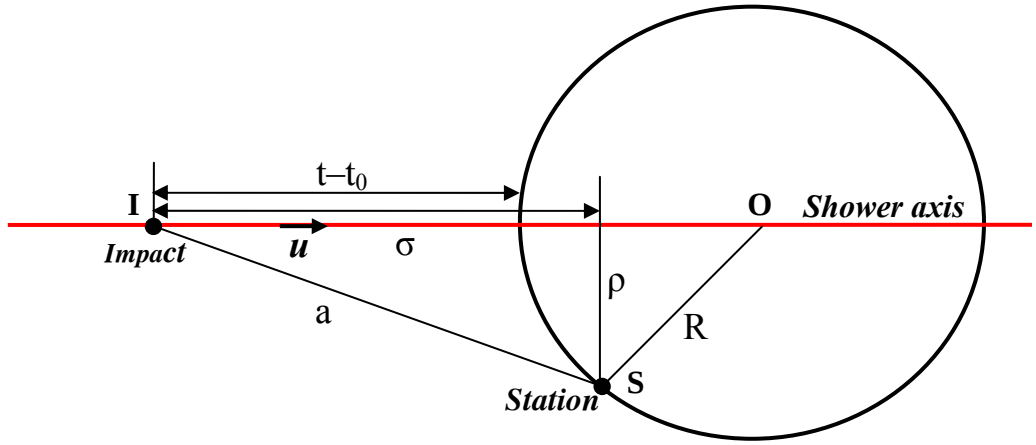

Figure 3.1 Definition of parameters used to describe an air shower. The drawing is in the plane containing the station and the shower axis. O and S are the center of the sphere and the station respectively and I is the impact on ground.

In a first step the space coordinates of the impact point, (x_0 , y_0 , z_0), are reconstructed as the coordinates of the centre of gravity of the stations hit using the

signals as weights. In a second step, a finer tuning can be made by searching for a best fit (using the radial and energy dependence of the lateral distribution function) at the same time as evaluating the energy. Here, however, we concentrate on the first step and the problem reduces to the evaluation of θ, φ, (or equivalently $\lambda = sin\theta\ cos\varphi$ and $\mu = sin\theta\ sin\varphi$), t_0 and C from the times of arrival t_i of the signal in at least four of the stations. From Figure 3.1, calling σ_i the projection on the shower axis of the vector joining the impact to station i

$$\vec{u} = (\lambda, \mu, cos\theta) \tag{3.1}$$

$$\sigma_i = a_i . \vec{u} = (x_i - x_0)\lambda + (y_i - y_0)\mu \tag{3.2}$$

where x_i and y_i are the coordinates of the detection stations (located on a flat horizontal ground at z_0=0, at the nodes of a triangular lattice with mesh size equal to 1.5 km).

Calling ρ_i the distance of a station hit to the shower axis we have

$$\rho_i^2 = a_i^2 - \sigma_i^2 = (x_i - x_0)^2 + (y_i - y_0)^2 - \sigma_i^2 \tag{3.3}$$

The basic relationship between t_i and the parameters of the showers is obtained from Figure 3.1 by splitting the segment OI in two different ways :

$$t_i - t_0 + R = \sigma_i + \sqrt{R^2 - \rho_i^2} \tag{3.4}$$

where $R=1/(2C)$ is the radius of the shower front.

Squaring (3.4) we obtain

$$([t_i - t_0] - \sigma_i)^2 + 2R([t_i - t_0] - \sigma_i) + \rho_i^2 = 0 \tag{3.5}$$

or equivalently

$$t_i = t_0 + \sigma_i - C[\ (\sigma_i - [t_i - t_0])^2 + \rho_i^2] \tag{3.6}$$

Writing $\alpha_i = [(\sigma - t)^2 + \rho^2]_i$ (3.7)

we find

$$t_i = t_0 + \lambda\ (x_i - x_0) + \mu\ (y_i - y_0) + C\ (-\alpha_i) \tag{3.8}$$

Equations (3.8), one for each station hit, allow for the evaluation of the four unknown shower parameters t_0 , θ, φ and C as long as there are at least 4 stations hit.

For $C = 0$, t_i is a linear function of λ, μ and t_0. In that case, they can be calculated analytically by minimizing $\chi^2 = \sum_i [t_i - t_0 - \lambda (x_i - x_0) - \mu(y_i - y_0)]^2 / (\Delta t_i)^2$.

Here, for simplicity, we take the measurement error Δt_i to be a constant (arbitrary taken as unity). However for $C \neq 0$, the α_i's being functions of λ, μ and t_0, the equations are no longer linear. But as $C = 0$ is a good first order approximation, it is still possible to solve equation (3.8) by iteration: set $C_0 = 0$, solve (3.8) analytically in λ, μ and t_0, calculate α_{i0} using Relation (3.7), solve (3.8) analytically in λ, μ, t_0 and C with $\alpha_i = \alpha_{i0}$, calculate $\alpha_i = \alpha_{i1}$ by putting the new values of λ, μ, t_0 and C into the Relation (3.7), iterate until it converges. In fact, the convergence is very rapid.

3.2 Monte Carlo simulation

In order to illustrate and check the procedure of geometric event reconstruction described above, a rudimentary simulation program (toy Monte Carlo) has been written.

In a first step shower axes are generated isotropic in space. This means with uniform φ and $\cos\theta$ distributions (between $-\pi$ and π and between $0.36 = \cos 69^\circ$ and 1.0 respectively). The curvature $C = 1/(2R)$ of the shower front is taken with a uniform distribution between 0 and 0.1 km^{-1}. The detector array covers a square area of 30×30 km^2. Impacts are generated uniformly in a smaller concentric square, 20×20 km^2, leaving a 5 km safety margin all around. The event time t_0 is taken with a uniform distribution between 0 and 10 km (all distances and times are measured in km).

In a second step, the response of the detector array is calculated according to the arithmetic described in the preceding paragraph. The arrival time of each station hit is deduced from the generated values of the parameters σ, ρ, C_0. The signal of each station hit is calculated by assuming that the particle density on the shower front decreases exponentially with ρ, namely $S_i = \exp(-\rho_i^2/\rho_0^2)$ with $\rho_0^2 = 2$ km^2. The number N_s of stations hit is calculated by requiring that their signals be greater than a given threshold.

In a third step, the impact is reconstructed as the centre of gravity of the stations hit using the signals as weights. In this same step, the shower parameters

are calculated in planar and curved approximation from Relations (3.7) and (3.8), by iteration as described above.

The fitted values of the four shower parameters θ, φ, t_0 and C were found identical to the generated values, providing evidence for the good performance of the iteration method described above. Figures 3.2a, 3.2b, 3.3a and 3.3b compare generated and reconstructed values of the impact coordinates for each of two threshold values, 10% and 1% the signal at the shower core. As expected a much better accuracy is achieved for the lower value of the threshold. Also shown in the figures are the number N_s of stations hit (above threshold) and its dependence on θ. Here again the results agree with expectation: there are on average 12.4 stations hit at high threshold and 24.3 stations hit at low threshold. Moreover, the number of stations hit increases trivially with $1/\cos\theta$.

This program has been used to reconstruct events collected using the four Cherenkov tanks installed on top of the laboratory roof as well as to study the systematic errors attached the energy measurement using the Auger surface detector array. However, these studies are beyond the scope of the present thesis and will not be described here.

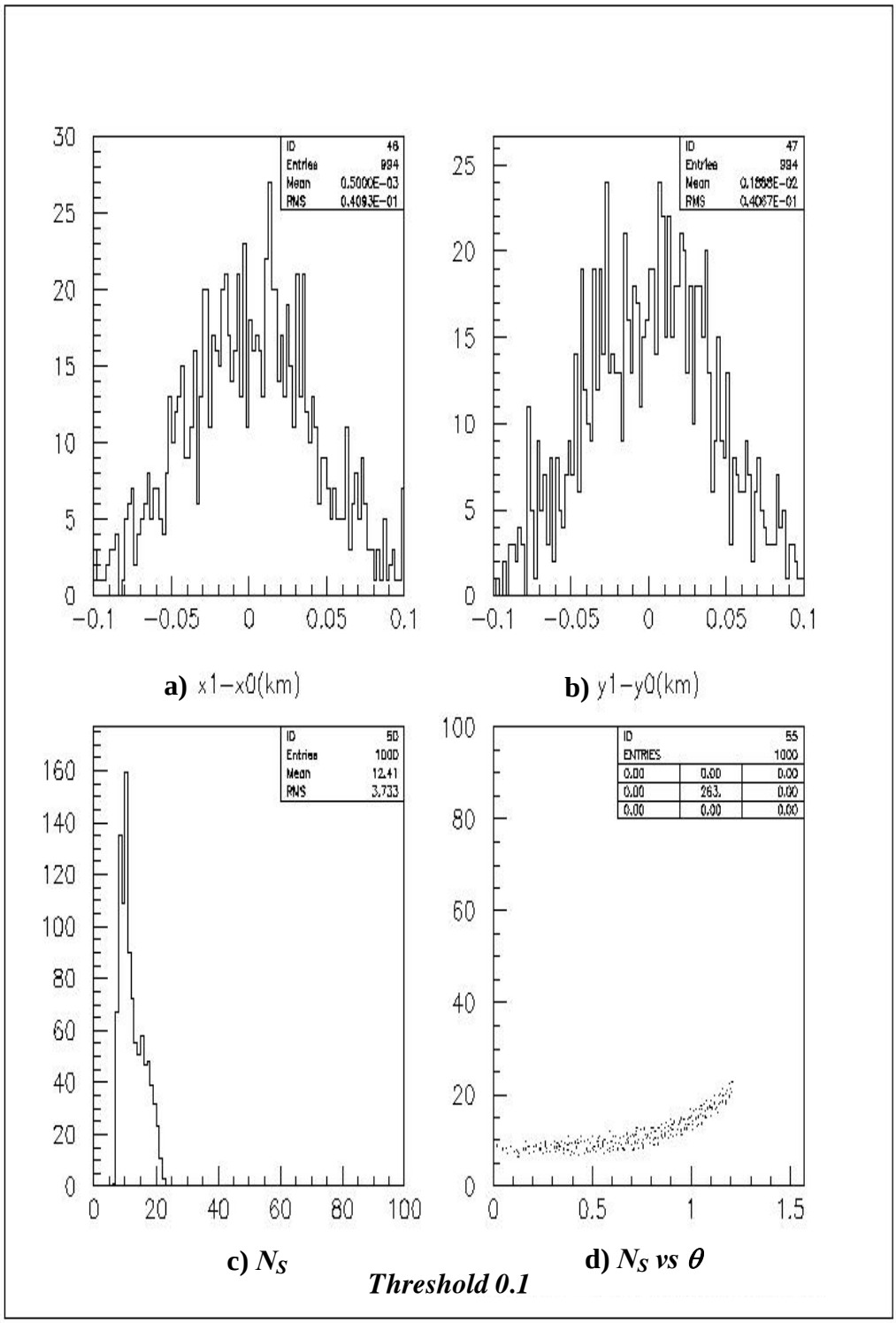

Figure 3.2: Threshold=0.1 a and b: distributions of the differences between reconstructed and generated impact coordinates. c and d: distribution of the number of stations hit and its dependence on θ.

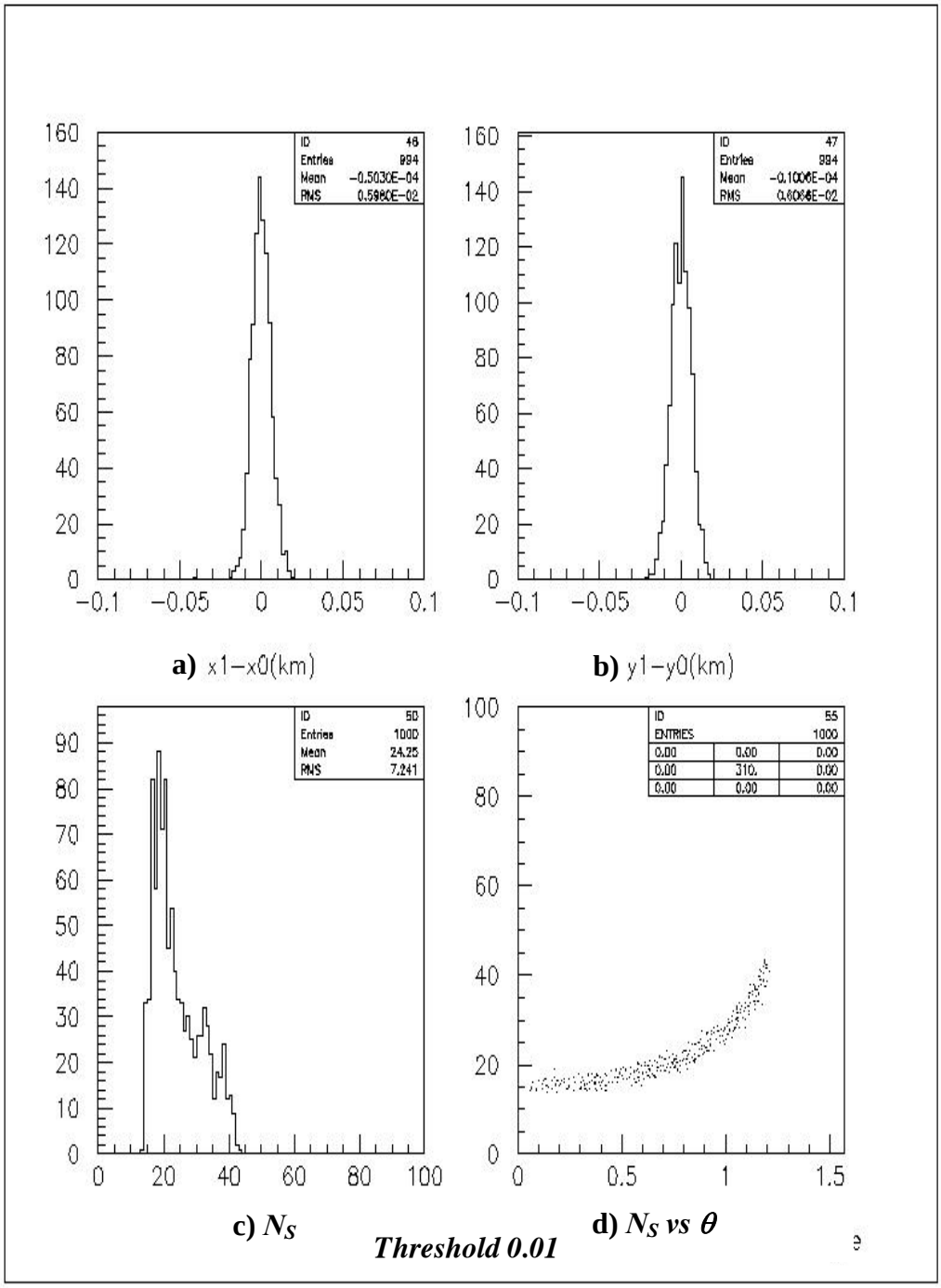

Figure 3.3: Threshold=0.01 a and b: distributions of the differences between reconstructed and generated impact coordinates. c and d: distribution of the number of stations hit and its dependence on θ.

Chapter 4

EVENT RECONSTRUCTION USING THE FLUORESCENCE DETECTOR

A program has been written and tested in order to study and understand the main features of the fluorescence detector and its response to showers. In order to do this we have developed a code that simulates the detector.

4.1 Shower reconstruction: principle of the method

A single eye is able to measure both the location of the shower axis in space and the shower energy. Locating the position of the shower axis in space is made in two steps. The first, straightforward step consists in fitting a line to the pattern of pixels hit: this fixes directly the position of the shower detector plane (SDP, defined in Figure 4.1) with an accuracy that scales with the pixel aperture.

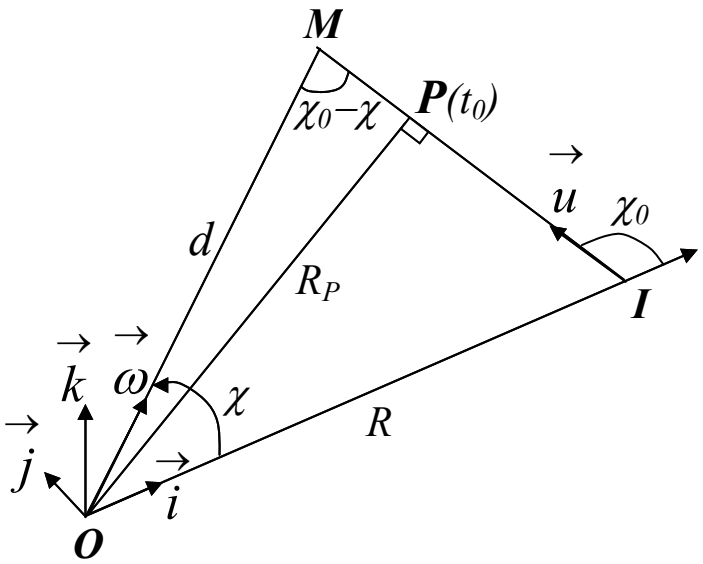

Figure 4.1: The eye O looks at the shower axis IM that crosses ground in I. OIM is the SDP. The unit vectors along OI, IM and OM are called ***i****,* ***u*** *and* ***ω*** *respectively. The unit vector along the vertical is called* ***k****. $OP=R_P$ is the shortest distance from the eye to the shower axis. OM=d and OI=R. The shower front passes P at time t_0 and M at time t. The angles χ and χ_0 are defined as* ***(i,ω)*** *and* ***(i,u)*** *respectively.*

The second step, locating the shower axis in the SDP, is far more delicate and relies on the time measurement. Each 100 ns slice centered on time t_i detects an amount of light ΔS_i emitted from a small shower segment spanning an atmosphere thickness Δa_i centered on an average thickness a_i as measured from the direction of view of the associated pixel(s). The position of the shower axis in the SDP is defined by two parameters: R_p and χ_0; R_p is the shortest distance from the eye to the shower axis and

χ_0 is the angle between the shower axis and the trace OI of the SDP on ground. Similarly, the axis of view of the pixel(s) associated with mean time t_i is defined by the angle χ_i that it makes with this trace.

The time taken by the light to reach the eye is

$t_i = t_0 - MP + MO = t_0 - R_P/\tan(\chi_0-\chi_i) + R_P/\sin(\chi_0-\chi_i)$, leading to the relation:

$$(t_i-t_0)/R_p = 1/\sin(\chi_0-\chi_i) - 1/\tan(\chi_0-\chi_i) = \tan([\chi_0-\chi_i]/2) \qquad (4.1)$$

Here, t_0 fixes the absolute time of arrival of the shower front in P and is of no interest to the present problem (it is however essential for binocular or hybrid detection in order to combine signals from different detectors): locating the shower axis in the SDP depends only on the time differences between different pixel signals. We see immediately from Relation (4.1) that the parameters t_0 and R_p are essentially measured respectively by a shift and a scaling in ordinate of the t_i *vs* χ_i relation, leaving the determination of χ_0 to rely on the measurement of its shape, in particular its curvature. As, in practice, this curvature is very small, the measurement of χ_0 is particularly delicate. We also see from Relation (4.1) that, to the extent that the range spanned by χ_i is small, R_p and χ_0 are anticorrelated, the product $R_p \tan([\chi_0 - <\chi_i>]/2)$ being equal to $<t_i> - t_0$.

Once R_p and χ_0 are known, a_i and Δa_i are easily calculated and the associated amount of fluorescence light is obtained by scaling the measured signal ΔS_i by the reciprocal of the detection solid angle and correcting it for the attenuation in the atmosphere, both operations depending on the distance $d_i = OM$ between the eye and the shower segment under consideration.

We see from Figure 4.1 that $d_i = R_P/\sin(\chi_0-\chi_i)$ and that the altitude z_i of M above ground is $z_i = d_i \vec{\omega}.\vec{k} = d_i \sin\chi_i \sin\Psi = R_P \sin\chi_i \sin\Psi / \sin(\chi_0-\chi_i)$ (4.2)

where Ψ is the angle between the SDP and ground (measured from the trace of the shower in the pixel plane). The relation between pressure p_i and altitude above sea level, $z_i + z_{ground}$, is known from atmospheric standard data. Here, for simplicity, we assume that it is a simple exponential of the form

$$p_i = p_{sl} \exp(-[z_i + z_{ground}]/z_{atm}) \qquad (4.3)$$

with a sea level pressure p_{sl} of 1000 g/cm^2 and z_{atm}=7.8 km.

Combining relations (4.2) and (4.3) we obtain

$$a_i = p_i / cos(\vec{u}, \vec{k}) = p_i / (sin\Psi sin\chi_0). \quad (4.4)$$

Having reconstructed the longitudinal shower profile, and extrapolated it outside the field of view when necessary, its integral is in principle proportional to the energy, the proportionality factor being obtained from shower simulations including state of the art knowledge of the laws obeyed by its development. In practice, it is convenient to fit the observed profile to some standard profile that depends essentially on two parameters, the atmosphere thickness a_{first} at which the first interaction occurs and that, $\Delta_{max}+a_{first}$, at which the shower reaches its maximum development. While Δ_{max} depends directly on energy, a_{first} is an indicator of the nature of the primary: heavier nuclei initiate their shower earlier than lighter nuclei do. Such a particularly simple standard profile is given by [11] as

$$ln\{\Delta S_i/\Delta a_i\} = ln\{E/\Delta_{max}\}+(\Delta_{max}/w)\, ln\{[a_i-a_{first}]/\Delta_{max}\}+(\Delta_{max}-[a_i-a_{first}])/w) \quad (4.5)$$

Here, E is the energy in GeV, w=70 g/cm^2 and Δ_{max} , the thickness separating the first interaction from the shower maximum, is parameterized as a linear function of the logarithm of the energy [12] as

$$\Delta_{max} = 107 \text{ g/cm}^2 + 67 \text{ g/cm}^2 \times log_{10}E. \quad (4.6)$$

In principle, the shower energy can be obtained from Δ_{max} as: E = 10**{(Δ_{max} -107)/67}. However, this determination is far less precise than that obtained from the integral of the shower profile. Note that in the PAO z_{ground} =1.4 km, implying that a 10^{20} eV vertical shower reaches maximum development on ground.

Finally, a_{first} has an exponential distribution with an interaction length Λ_{int} calculated from a proton-air interaction cross-section σ_{int} parameterized [12] as a function of energy as

$$\sigma_{int} = 150 \text{ mb} + 40 \text{ mb} \times log_{10}E. \quad (4.7)$$

4.2 Monocular observation: locating the shower axis in the SD plane

4.2.1 The method

In the present section we study in some detail the properties of Relation (4.1) that is used to calculate the position of the shower axis in the SDP in case of monocular observation. For simplicity we consider showers located in a vertical SDP (Ψ=90°) and assume that they cross the whole field of view (from χ_{up}=28° to χ_{down}= 0°). Their energy is irrelevant to the present considerations. The only variable parameters are therefore R_P and χ_0 . In order to compare showers that are at similar distances from the eye, we fix their distance in the middle of the field of view (χ_{mean}=14°) to be $R \sin \chi_0 / \sin(\chi_0 - \chi_{mean})$=10 km. Finally we assume that times are exactly measured in bins of 100ns. For each shower we obtain this way a set of (t_i, χ_i) pairs which we may modify at will in order to simulate measurement errors. To calculate R_P , t_0 and χ_0 from these data we minimize their χ^2 to Relation (4.1). Writing $u_i=\tan(\chi_i/2)$ and $u_0=\tan(\chi_0/2)$, Relation (4.1) reads $(t_i - t_0)(1+u_i u_0)=R_P (u_0 - u_i)$ that can be rewritten as

$$\{t_0 + R_P u_0\} + u_i \{t_0 u_0 - R_P\} - t_i u_i \{u_0\} = t_i \qquad (4.8)$$

Relation (4.8) is linear in the parameters inserted in curly brackets: its χ^2 can be minimized exactly by solving the linear system of three equations expressing that its derivative with respect to each of the three parameters cancels.

4.2.2 Effect on the χ_0 and R_P measurements of systematic errors on χ_i

Shifting all χ_i's by a same quantity δ obviously results in an identical shift for χ_0 , the other parameters being unaffected. Similarly, shifting each χ_i by a quantity $\delta_i = \delta (1 - \chi_i / \chi_{mean})$ results in small changes in both R_P and χ_0 : the ratio $\Delta R_P / R_P \delta$ cancels for χ_0 = 104° (showers normal to the mean axis of view) and reaches –4 at χ_0 =30° and 3 at χ_0=150° ; the ratio $\Delta\chi_0/\delta$ is negative and of the order of –3 over the whole field of view.

However, shifting each χ_i by a quantity $\delta_i = \delta (1 - \chi_i / \chi_{mean})^2$ results in dramatic changes in both R_P and χ_0 , approximately proportional to δ. This is illustrated in Figure 4.2 where the relative shifts $\Delta R_P/R_P\delta$ and $\Delta\chi_0/\delta$ are shown as a function of χ_0. The shifts in χ_i are amplified by very large factors reaching over 30 in the R_P case and over 60 in the χ_0 case.

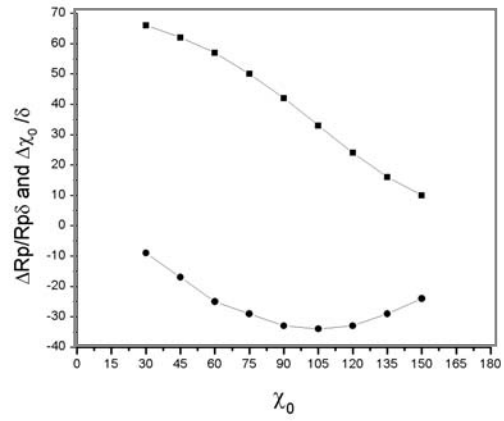

Figure 4.2: Dependence of $\Delta R_P / R_P\ \delta$ (circles) and $\Delta\chi_0 / \delta$ (squares) on χ_0 (degrees) for quadratic errors of the form $\delta_i = \delta(1-\chi_i/\chi_{mean})^2$.

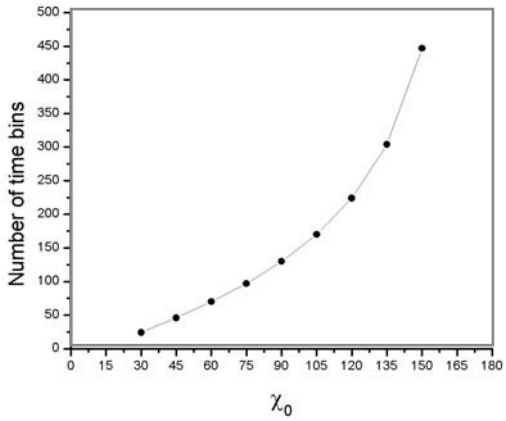

Figure 4.3: Dependence on χ_0 of the number N_{bin} of 100ns time bins spanned by the shower.

This extreme sensitivity to errors having a quadratic dependence on χ is the dominant feature of Relation (4.1). It is easily understood by developing it around χ_{mean} :

$$(t-t_0)/R_p=\{\tan((\chi_0-\chi_{mean})/2)-\tan((\chi-\chi_{mean})/2)\}/\{1+\tan((\chi_0-\chi_{mean})/2)\tan((\chi-\chi_{mean})/2)\}$$

Defining $\tau_0 = \tan((\chi_0-\chi_{mean})/2)$ and $\tau = \tan((\chi-\chi_{mean})/2)$ we have to second order in τ:

$$(t-t_0)/R_p = (\tau_0-\tau)(1-\tau_0\tau+[\tau_0\tau]^2) = \tau_0-(1+\tau_0^2)\tau+\tau_0(1+\tau_0^2)\tau^2$$

Namely, in the plane (t, τ), $t = [t_0+R_p\tau_0]-[R_p(1+\tau_0^2)]\tau+[R_p\tau_0(1+\tau_0^2)]\tau^2$ (4.9)

In the linear approximation, we only measure $t_0+R_p\tau_0$ and $R_p(1+\tau_0^2)$: we need to measure the curvature to disentangle R_p from τ_0.

Defining a slope $S=-R_p(1+\tau_0^2)$ and a curvature $C=R_p\tau_0(1+\tau_0^2)$, we have $\tau_0=-C/S$ and $R_p=-S^3/(S^2+C^2)$. The constant term does nothing but to define t_0. For zero curvature, the slope measures R_p. And for a small curvature ($C<<S$), the slope measures essentially R_p and the curvature measures τ_0. In particular, any source of error that may introduce a spurious curvature in Relation (4.9) will directly affect the measurement of τ_0 and therefore of the other two variables.

Note that for $R_p=0$, namely when the shower points to the eye, all the light reaches the eye at a same time t_0 and hits a same pixel : this is the signature of $R_p=0$ and χ_0 is simply equal to the χ of that pixel in this case. Indeed the time span, $t(\chi_{down})-$

$t(\chi_{up})$, depends strongly on χ_0 as illustrated in Figure 4.3. The smaller it is, the poorer the χ_0 measurement.

As a further illustration of the properties of Relation (4.1) we have studied the effect of uncorrelated Gaussian errors having an *rms* value δ (but truncated at $\pm 0.7^o$ in order to stay within a pixel size). In spite of the errors being random, large shifts result in both R_P and χ_0. The rms value of the $\Delta\chi_0/\delta$ distribution is found to be approximately inversely proportional to the number N_{bin} of 100ns bins spanned by the shower with $N_{bin} \times Rms(\Delta\chi_0/\delta) \sim 1300$. Figures 4.4 and 4.5 illustrate the case of a vertical shower ($\chi_0=90^o$): Figure 4.4 shows the correlation between $\Delta R_P / R_P \, \delta$ and $\Delta\chi_0/\delta$ and Figure 4.5 shows the distribution of $\Delta\chi_0/\delta$. Not only very large errors may occur – in the case of χ_0 typically 50 times as large as the average error on χ_i – but there is also a systematic shift on both the R_P and χ_0 measurements.

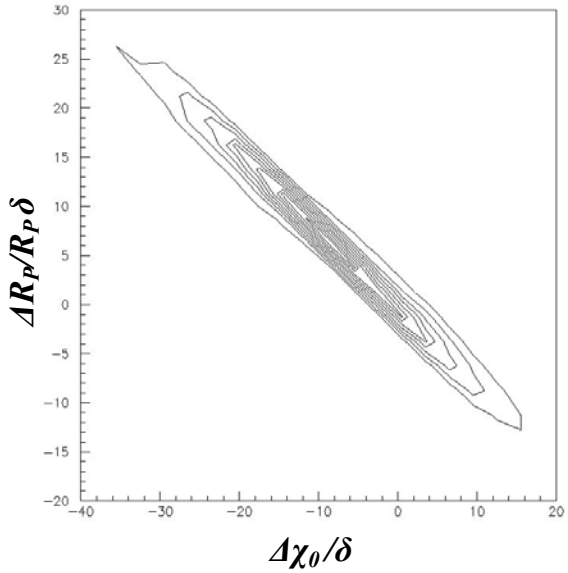

Figure 4.4: Correlation between $\Delta R_P/R_P\delta$ (ordinate) and $\Delta\chi_0/\delta$ (abscissa) for $\chi_0=90^O$ and for Gaussian truncated errors (see text).

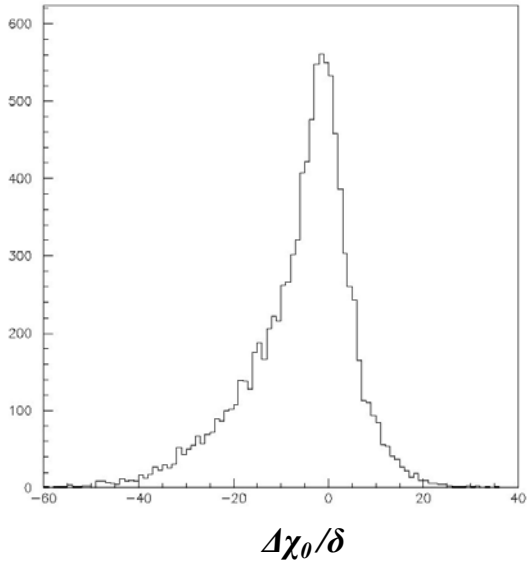

Figure 4.5: Distribution of the shifts $\Delta\chi_0/\delta$ induced by Gaussian errors for $\chi_0=90^o$ (see text).

4.2.3 Resulting distortions of the shower profile

By differentiating Relation (4.2) with respect to R_P and χ_0 we can study the distortion of the shower profile resulting from errors on the location of the shower

axis within the SDP. For simplicity we assume that the SDP itself is exactly reconstructed. We obtain:

$$dz_i/z_i = dd_i/d_i = dR_P/R_P - cotan(\chi_0 - \chi_i)\, d\chi_0 \qquad (4.10)$$

and from Relations (4.3) and (4.4) $da_i/a_i = dp_i/p_i - cotan\ \chi_0\ d\chi_0 = -dz_i/z_{atm} - cotan\ \chi_0\ d\chi_0$

$$da_i/a_i = -[z_i/z_{atm}]\ dR_P/R_P + ([z_i/z_{atm}]\ cotan(\chi_0 - \chi_i) - cotan\ \chi_0)\ d\chi_0 \qquad (4.11)$$

There are two kinds of distortions induced by errors on R_P and χ_0 : distortions of the scale of atmospheric thicknesses (abscissa) and distortions of the light signal (ordinate). The former are directly obtained from Relation (4.10) while distortions of the light signal result from errors on the detection solid angle and on the atmospheric light attenuation, themselves induced by errors on the measurement of d.

Distortions of the atmospheric thickness scale are constrained by their ground value, $[da/a]_{ground} = -\ cotan\ \chi_0\ d\chi_0$. On ground an error on R_P causes a parallel translation of the shower axis and induces therefore no error on a while an error on χ_0 trivially does as a is inversely proportional to $sin\ \chi_0$. As a result, such distortions will only be important when large z values are in the field of view, namely for very inclined showers pointing in the eye direction. However, they will have little effect on the energy measurement to the extent that the shower profile is well contained within the field of view: in such cases the energy measurement is dominated by the integrated light signal, *i.e.* by the first term in Relation (4.5), that is independent of the atmospheric thickness scale. Only in the case where the longitudinal profile needs to be extrapolated outside the field of view will such errors be of relevance to the energy measurement. On the contrary, the measurement of a_{first} is directly affected by distortions of the atmospheric thickness scale in the region of early shower development, which are again important in the case of inclined showers pointing toward the eye.

Distortions of the light signal are instead of direct relevance to the energy measurement. The measured signal is inversely proportional to d^2 and has an additional exponential dependence on d due to light attenuation in the atmosphere. A 1% error on d induces therefore an energy error in excess of 2% . On ground, Relation (4.10) reads $dd/d = dR_P/R_P - cotan(\chi_0)\, d\chi_0$.

For a vertical shower, the relative error on d equals that on R_P while for inclined showers the two terms of Relation (4.10) may add or subtract depending whether the shower points away from the eye or toward it. When the errors on R_P and χ_0 have a same origin and are anticorrelated, as in the case of the showers discussed in Section 4.2.2, the error on d is more important for inclined showers pointing to the eye.

4.3 Measuring the shower energy

An accurate measurement of the shower energy relies on an accurate measurement of the longitudinal shower profile and on a precise knowledge of the relation between energy and amount of fluorescence light. Which is more important depends on what one is after. For example, in the GZK region, establishing whether or not there is a cut-off does not require an excellent knowledge of the energy scale but does require an excellent control over systematic errors. If there is such a cut-off and if one has enough statistics and an excellent control over systematic errors, one will see it and one might then argue with some mischief that it could be used to calibrate the energy scale in a region where accelerator data are lacking. Without going that far, we simply wish to underline the need for an excellent control over systematic errors.

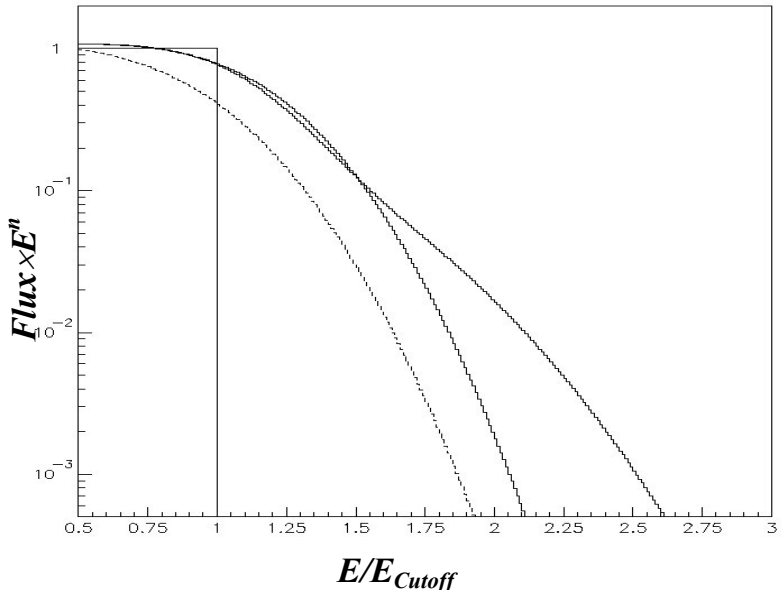

Figure 4.6 : Simulation of measured fluxes (times E^n) for an initial E^{-n} spectrum abruptly cut off at $E_{cutoff}=1$ (see text) as a function of energy relative to cutoff. The full lines are for n=3 and 30% errors, either single Gaussian (narrower curve) or double Gaussian (wider curve). The dotted line is for n=0 and single Gaussian errors.

We illustrate this point by considering an E^{-n} spectrum abruptly cut-off at E_{cutoff} and showing how it can be distorted by systematic errors. Figure 4.6 shows simulated experimental spectra multiplied by E^n obtained for measurement errors having an *rms* value of 30%. For n=3, the error distribution is represented by a single Gaussian in one case, by the sum of two Gaussians, one twice as large as the other, in the other case. To have less than a 1% probability to measure an event of a given energy or higher, one needs to go to f=1.58 times the cut-off in the single Gaussian case and to f=1.76 times the cut-off in the double Gaussian case, illustrating the effect of tails in the error distribution. The dotted line is for n=0, a step function. Here, f=1.37: at variance with the n=3 case, the smearing is smaller, illustrating a well known property of steeply falling spectra. These trivial remarks underline the importance of understanding well the shape of the error distribution and the danger of simply assuming that it is a Gaussian.

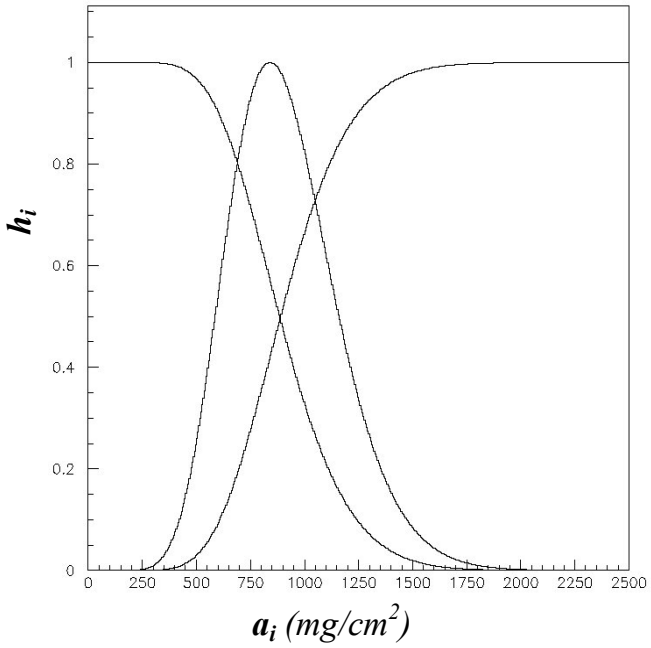

Figure 4.7: The shower profile used in the present study and the fractional losses f_{early} and f_{late} and as functions of the atmosphere thickness traversed (mg/cm^2).

A potential source of systematic errors is the need for an extrapolation of the observed profile outside the field of view. This may be studied using a profile of the form (4.5) and assuming that only a portion of the profile is observed, leaving unobserved energy fractions f_{early} and f_{late} corresponding respectively to the early and late parts of the shower development. The profile used here, h_i vs a_i , is of a shower of 10^{20}eV (Δ_{max} =840g/cm^2). The h_i scale is normalized to have h_i=1 at maximum (where a =Δ_{max}). Its dependence on a is illustrated in Figure 4.7 together with the fractional losses f_{early} and f_{late} . For a given field of view, a sliding window of width w_{field} and starting at thickness a_{field} , we calculate the χ^2 describing the deviation between the

undistorted profile (Δ_{max} , a_{first}) and a distorted profile ($\Delta_{max}+\delta\Delta_{max}$, $a_{first}+ \delta a_{first}$). The error ellipse $\chi^2=1$ gives the errors $\Delta(a_{first})$ and $\Delta(\Delta_{max})$ on the measurements of a_{first} and Δ_{max} as well as the correlation between them. These errors are a measure of the quality of the measurement and of its sensitivity to the width and location of the sliding window. They are shown in Figures 4.8 and 4.9 as a function of a_{field} for three values of w_{field} , 100g/cm^2, 200g/cm^2 and 300g/cm^2. Their qualitative behavior does not much depend on the exact value of the uncertainties used in the calculation of the χ^2. Here they were taken of the form $\Delta h_i=0.001+0.01h_i$ (remember that h is normalized to unity at maximum). The features visible on Figures 4.8 and 4.9 are easily understood: the errors on a_{first} and Δ_{max} decrease when the width w_{field} of the field of view increases; the error on a_{first} becomes larger when moving away from the early part of the shower development; the error on Δ_{max} is minimal when the field of view covers the shower maximum.

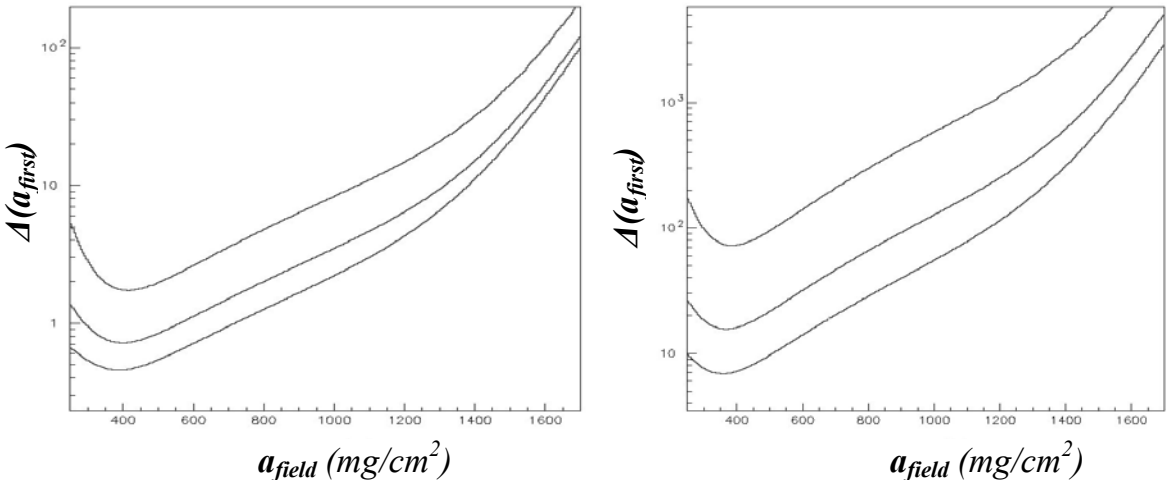

Figure 4.8 Dependence of $\Delta(a_{first})$ on a_{field} for w_{field} =100 (up), 200 (middle) and 300 (down) g/cm^2 . On the left, both the shape and the intensity of the profile are considered, on the right only the shape.

The error on Δ_{max} is usually small because Δ_{max} is essentially fixed by the intensity of the light and depends only weakly on the shape of the profile. On the contrary, the error on a_{first} is typically an order of magnitude larger because the measurement of a_{first} is not directly affected by the h scale but only by the shift of the profile along the abscissa.

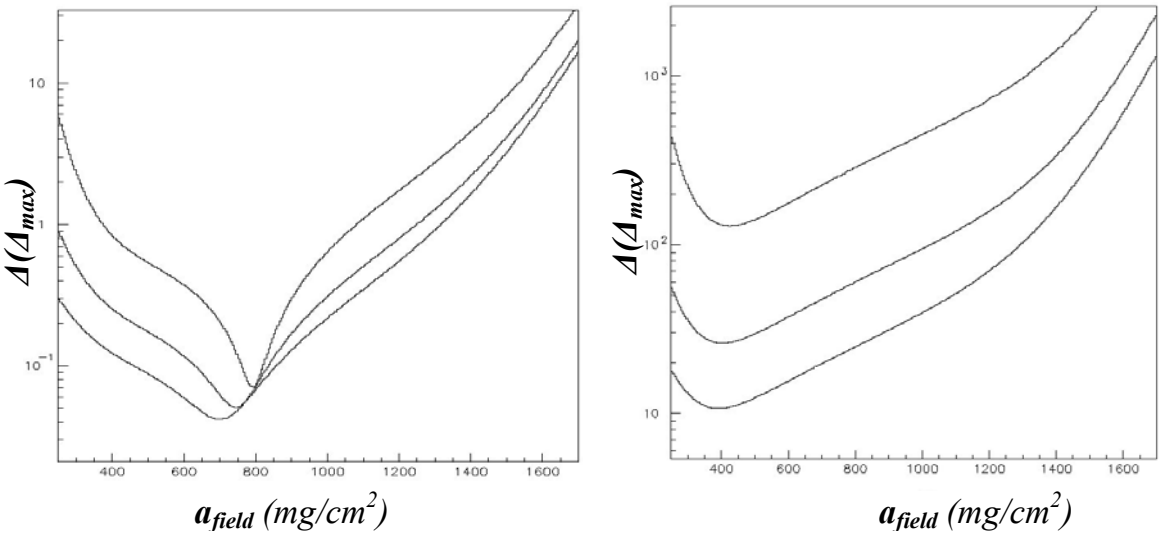

Figure 4.9 Dependence of $\Delta(\Delta_{max})$ on a_{field} for w_{field} =100 (up), 200 (middle) and 300 (down) g/cm^2 . On the left, both the shape and the intensity of the profile are considered, on the right only the shape.

It is interesting to evaluate the deterioration of the accuracy when one considers only the shape of the profile and disregards its intensity. The results of such calculations are shown on the right parts of Figures 4.8 and 4.9. The error on Δ_{max} increases by two orders of magnitude, illustrating the comment that was just made, and that on a_{first} by one order of magnitude.

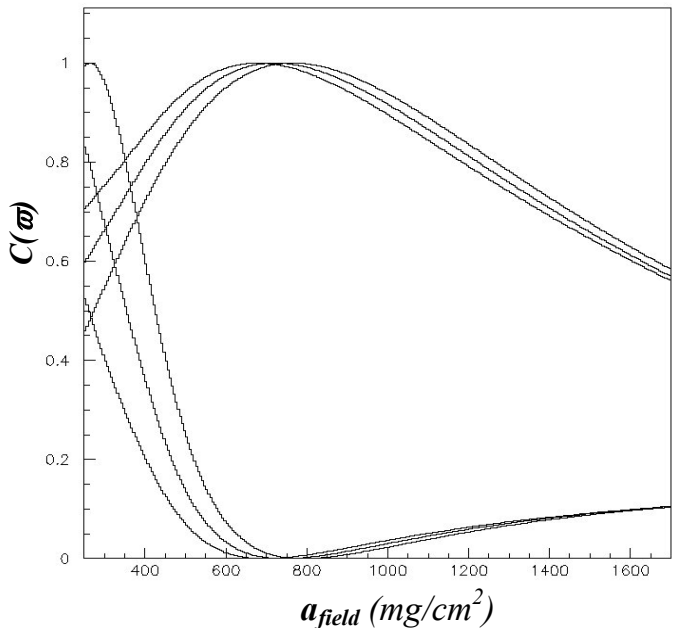

Figure 4.10 Correlation $C(\varpi)$ between the measurements of a_{first} and Δ_{max} . For the three lower curves, both the shape and the intensity of the profile are considered, for the three upper curves only the shape.

Finally, Figure 4.10 illustrates the correlation between the two measurements. It shows the dependence of $C(\varpi)=\sin^2(2\varpi)$ on a_{field} where ϖ defines the orientation of the major axis of the error ellipse. C is a measure of the correlation between the two measurements. When both the

intensity and the shape of the profile are considered the correlation is weak except for low values of a_{field} when the field of view covers only the early part of the shower development. In particular, when the field of view covers the maximum of the shower development, Δ_{max} is essentially fixed by the intensity measurement and a_{first} is then obtained from the measurement of the value of a at which the maximum occurs: in such a case there is no correlation between the two measurements. On the contrary, when the field of view covers the early part of the shower development, an increase of Δ_{max} is easily compensated by an increase of a_{first}. When the shape of the profile is considered alone the correlation is much stronger and reaches a maximum when the field of view covers the maximum of the shower development. Indeed, for a locally flat profile, one can choose Δ_{max} as one wishes and a_{first} is then exactly determined: the two measurements are maximally correlated.

4.4 Hybrid detection

The elementary considerations presented in the preceding sections have shown that the field of view should offer a broad coverage in both time span and atmosphere thickness traversed in order to achieve an accurate measurement. Broad time coverage is essential in monocular observation; however, even so, monocular measurements remain of much lesser quality than binocular or hybrid measurements.

Binocular detection allows for an accurate positioning of the shower axis when the two SDP's make a large angle: the time information becomes almost irrelevant in such a case. However, many other sources of uncertainties that are inherent to the fluorescence detection method, such as errors in the light-energy calibration and the attenuation in the atmosphere, are still at play. For this reason we restrict the present discussion to the case of hybrid detection: in addition of allowing for an accurate location of the shower axis, it offers a completely independent measurement of the shower energy with very different sources of possible systematic errors. This feature makes hybrid detection particularly attractive.

The question we ask in the present section is to which extent are fluorescence and surface detections compatible, can hybrid events be accurately measured in both detectors? Indeed, it might be that showers benefiting of a broad time and thickness coverage in the fluorescence detector would fall outside the acceptance of the surface detector array (SDA). As in the previous sections, we do not attempt a

precise and detailed description of the problem but aim simply at identifying the relevant parameters and understanding the main features. For simplicity, following the broad lines of the PAO design, the SDA is taken to cover a circle having a radius of 30 km and four equidistant eyes are located on its circumference and look toward its centre. The field of view of each eye covers 180^o in azimuth, 28^o in elevation and the depth of field is 30 km. A shower is considered to be detected by the SDA if and only if its axis impacts ground within the area of the circle. In practice, any shower detected in the SDA is seen in one of the four eyes. It is therefore sufficient to study showers that are seen in one of the eyes. Their energy is fixed at 10^{20}eV and their zenith angle θ is taken to have a uniform cosine distribution.

Figure 4.11 shows distributions of the distance ρ of the shower impact on ground to the centre of the SDA circle measured in units of its radius. Namely showers having $\rho<1$ are detected by the SDA and showers having $\rho>1$ are not.

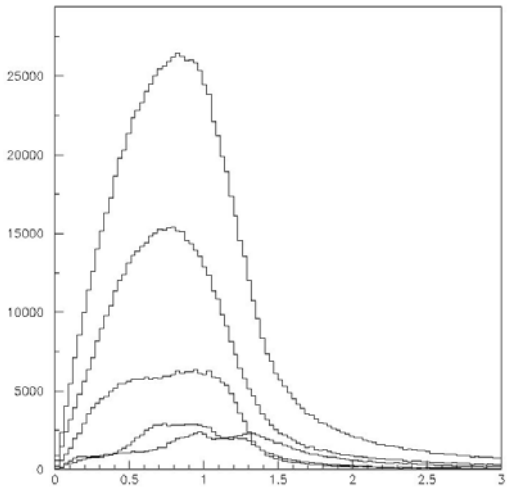

Figure 4.11a ρ distributions of various shower samples. From top to bottom: all showers, w_{field}>800g/cm^2, between 600 and 800g/cm^2, between 400 and 600g/cm^2 and <400g/cm^2.

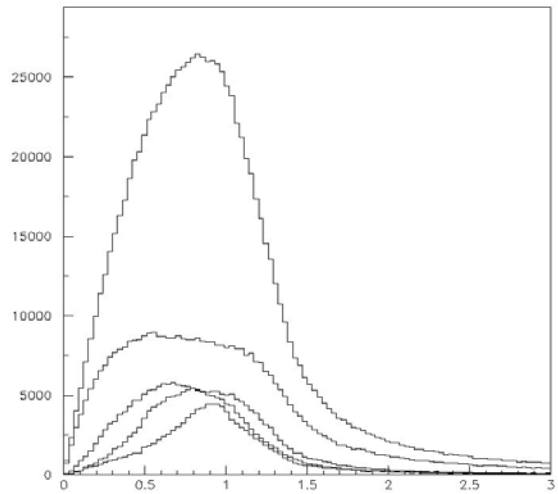

Figure 4.11b ρ distributions of various shower samples. From top to bottom: all showers, t_{field}>13km, between 7 and 13km, between 3 and 7km and <3km.

About 2/3 of the events seen in the eye are also seen in the SDA and are therefore hybrids. Also shown in Figure 4.11 are ρ distributions of various sub samples of the generated showers. Figure 4.11a is for different slices of w_{field}, the atmosphere

thickness covered by the field of view, and Figure 4.11b is for different slices of t_{field}, the time span covered by the field of view.

Figure 4.12 shows the *cos(θ)* and *φ* distributions, where *θ* and *φ* are the zenith angle and respectively azimuth of the shower axis, for showers having ρ <1 and ρ >1 respectively. Most of the showers that are detected by the eye but miss the SDA have large zenith angles and preferably fly toward the eye, that is have small values of *cos(θ)* and *φ* values that are enhanced around 0^o and depressed around 180^o.

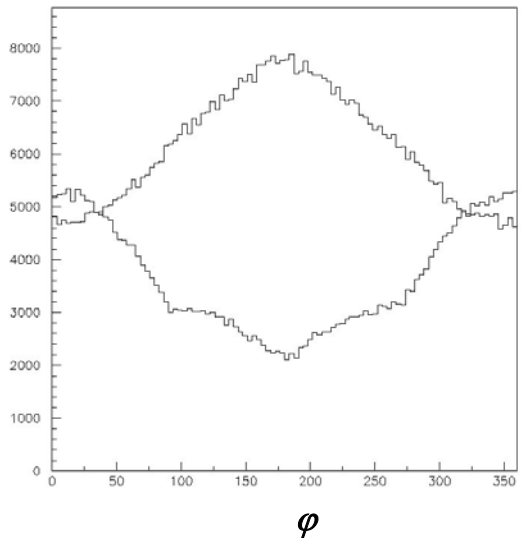

Figure 4.12a φ distributions of showers having ρ <1 (upper curve) and ρ >1 (lower curve) respectively.

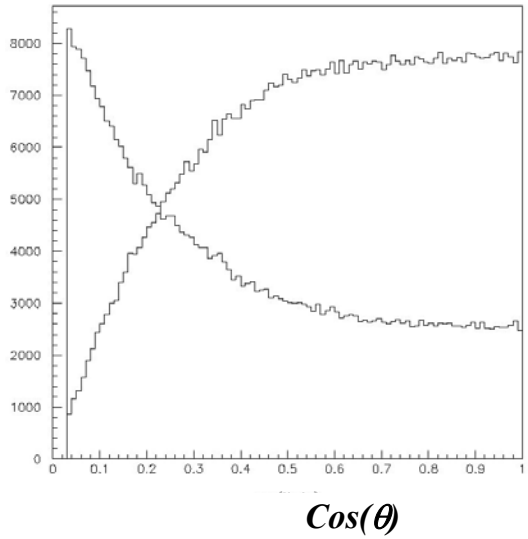

Figure 4.12b θ distributions of showers having ρ <1 (upper curve) and ρ >1 (lower curve) respectively.

The distributions in atmosphere thickness (w_{field}) and time span (t_{field}) covered by the field of view are illustrated in Figure 4.13 showing the distribution of the showers in the (w_{field}, t_{field}) plane for each of the two populations, ρ>1 and ρ<1. The showers that are missed by the SDA are clearly seen to populate low values of w_{field}.

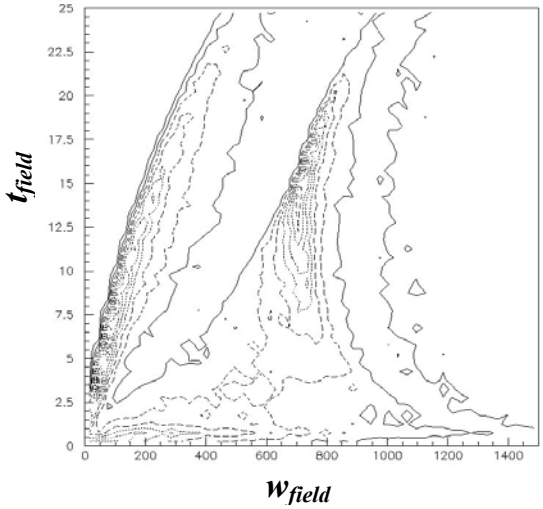

Figure 4.13a Distribution of the showers in the (w_{field}, t_{field}) plane for showers having $\rho>1$

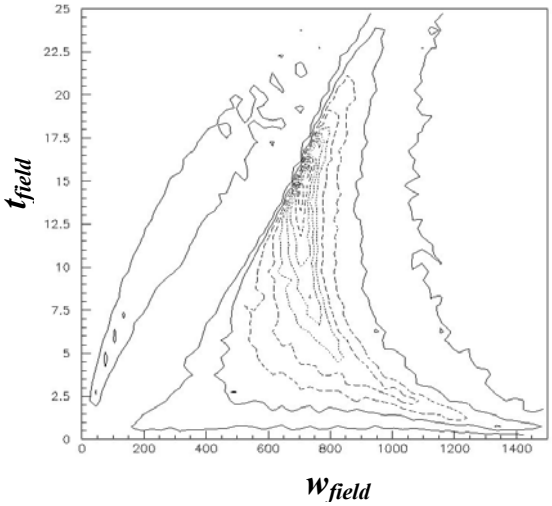

Figure 4.13b Distribution of the showers in the (w_{field}, t_{field}) plane for showers having $\rho<1$

An accurate energy measurement implies a good coverage on either side of the shower maximum. Figure 4.14 shows the ρ distribution of showers having a window of at least ±300 g/cm^2 on either side of the shower maximum within the field of view (third curve from top). 24% of all hybrids fall in this category. An accurate measurement of a_{first} requires instead a good coverage of the early part of the shower development. The ρ distribution of showers having a window of at least 300 g/cm^2 in the first 600 g/cm^2 of the shower development is also displayed on Figure 4.14 (second curve from top). 45% of all hybrids fall in this category. Showers satisfying both conditions are also shown (fourth curve from top). They amount to 11% of all hybrids.

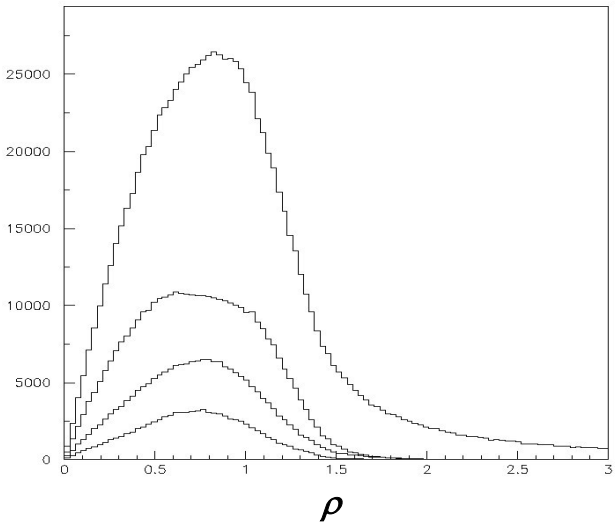

Figure 4.14 ρ distributions of various shower samples. From top to bottom: all showers, good a_{first} measurement, good energy measurement, both (see text).

SUMMARY AND PERSPECTIVES

The present work has concentrated on discussions of the methods used in the Pierre Auger Observatory to reconstruct showers induced by Ultra High Energy Cosmic Rays with particular emphasis on the sources of systematic errors that may affect the energy measurement. The systematic use of very simple simulation models and techniques has allowed for a clear understanding of the most relevant effects and for an easy identification of the parameters that define the quality of the energy measurement. Such a study needs to be completed by more detailed calculations using the very sophisticated simulation programs available to the Auger Collaboration. However such detailed studies are far less transparent and less convenient to interprete. Moreover the present study serves as a useful guide to an efficient use of the more sophisticated programs.

More time and effort were devoted to the study of the measurements performed in the fluorescence detector than in the surface detector. The reason is that the author is more closely associated with the former and will do his PhD work in collaboration with the Catania (Sicily) group of the PAO Collaboration, a group specialized in FD studies. In the SD case, the difficulty resides mostly in the indirect nature of the energy measurement that needs to be deduced from the transvere distribution of the density of secondaries on ground. A general and subtle problem is to understand how shower fluctuations may affect the energy measurement in such a case. While affecting also the longitudinal profile, they affect very little its integral and the calorimetric measurement offered by the FD is not expected to suffer of shower fluctuations as is the SD measurement. One of the tasks presently undertaken by the author is consequently a study of the effect of shower fluctuations on the longitudinal and tranverse shower profiles, with particular emphasis on the implications concerning the SD energy measurement and the systematic errors that affect it.

Among the main results of the present study we may mention the identification of parameters that are relevant to the assessment of the quality of the measurements performed, such as the spans in time and in atmosphere thickness covered by the field of view of the FD eyes.

The difficulty of locating accurately the shower in the shower-detector plane in the case of monocular observation has been discussed in some detail, pointing to the importance of making binocular, or better hybrid observations. The compatibility between fluorescence and surface detections was briefly commented upon and found to be very good in the PAO design. Considerations on the necessity to extrapolate the observed shower profile outside the field of view have shed some light on the different requirements implied by a good energy measurement and a good evaluation of the nature of the primaries.

The problems arising when inferring the shower energy from the amount of light detected are major and have been discussed in detail in the literature. They include, among others, the subtraction of direct and scattered Cherenkov light and the calibration of the energy scale. While difficult to solve, they are in principle easy to understand, this is why they were not considered in the present study. A major advantage of hybrid detection is that such problems are completely absent from SD detection. However, SD detection has its own difficulties, essentially alien to fluorescence detection.

REFERENCES

[1] M. Nagano and A.A. Watson, Rev. Mod. Phys. 72 (2000) 689.

[2] K. Greisen, Phys. Rev. Lett. 16 (1966) 748,
Z.T. Zatsepin and V.A. Kuzmin, Zh. Eksp. Teor. Fiz. Pis'ma Red. 4 (1966) 144.

[3] The Auger Collaboration, Nucl. Instr. Meth. A 523, 50 (2004).

[4] J.W. Cronin, The Highest Energy Cosmic Rays, talk presented at TAUP 2003, Seattle, USA.

[5] E. Parizot et al., editors, Physique et Astrophysique du rayonnement cosmique, Goutelas 2003, and references therein.

[6] M. Hillas et al., 11th ICRC (1969) EAS-35.

[7] M. Hillas et al., 12th ICRC (1969) EAS-18.

[8] G. Medina-Tanco, in the proceedings of ICRC 2005.

[9] R. Coy, Astroparticle Physics 6 (1997) 263.

[10] R.M. Baltrusaitis et al., Nucl. Inst. Meth. A240 (1985) 410,
D. Bird et al., Nucl. Inst. Meth., A349 (1994) 592,
D. Bird et al., Astrophys. J. 424 (1994) 491,
G. Davidson and R. ONeil, J. Chem. Phys. 41 (1964) 3946.

[11] P. Sokolsky, Am. Inst. Phys. Conf. Proc. 433 (1998) 65.

[12] T. K. Gaisser, AIP Conf. Proc. 558 (2001) 27.

[13] “The Pierre Auger Observatory Progress and First Results”, Pierre Auger Collaboration, Proceedings – 29th ICRC, Pune, India (2005).

[14] T.K. Gaisser, “Cosmic rays and Particle Physics”, Combridge University Press (1990).